Graphical Abstract

Understanding the Catalytic Chemisorption of the Cyanogen Chloride via Breakthrough Curve and Genetic Algorithm

Jaeheon Lee, Jaekyung Bae, Junemo Koo, Keunhong Jeong, Sang Myeon Lee, Heesoo Jung, Min-Kun Kim

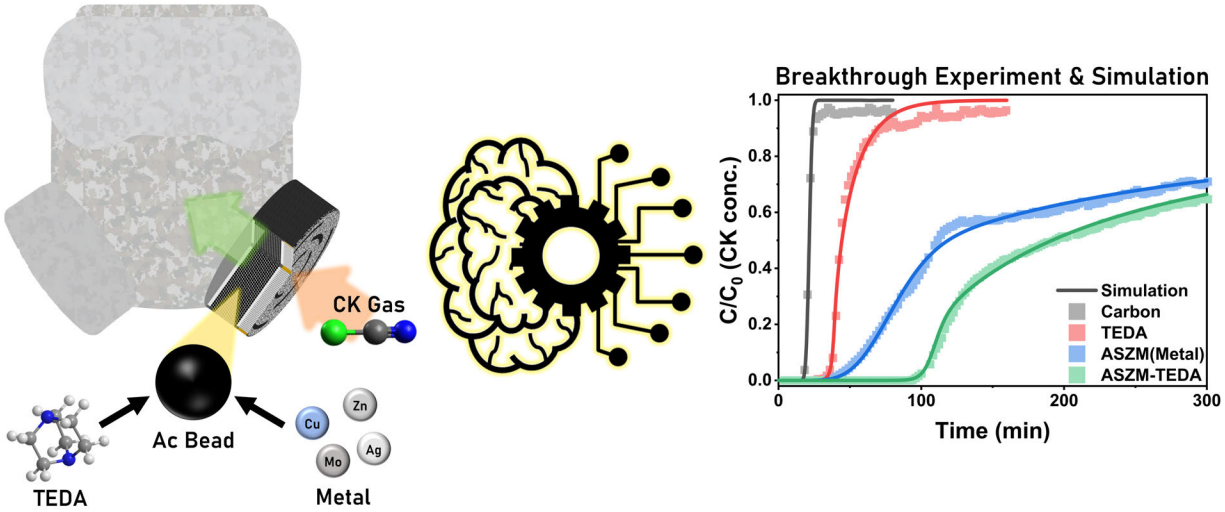

Highlights

Understanding the Catalytic Chemisorption of the Cyanogen Chloride via Breakthrough Curve and Genetic Algorithm

Jaeheon Lee, Jaekyung Bae, Junemo Koo, Keunhong Jeong, Sang Myeon Lee, Heesoo Jung, Min-Kun Kim

- Hydrolysis of CK within the metal-triethylenediamine complex was deeply studied
- TEDA accelerated the catalytic reaction of metal with CK by forming a water complex
- Breakthrough experiment and reaction-convection-diffusion equation were compared based on the genetic algorithm
- First study to analyze chemisorbed breakthrough behavior in depth

Understanding the Catalytic Chemisorption of the Cyanogen Chloride via Breakthrough Curve and Genetic Algorithm

Jaeheon Lee[a,1], Jaekyung Bae[a], Junemo Koo[b], Keunhong Jeong[c], Sang Myeon Lee[a], Heesoo Jung[a], Min-Kun Kim[a,*]

[a] *Chem-Bio Technology Center, Agency for Defense Development, Daejeon, 34186, Republic of Korea*
[b] *Department of Mechanical Engineering, Kyung Hee University, Yongin, 17104, Republic of Korea*
[c] *Department of Chemistry, Korea Military Academy, Seoul, 01805, Republic of Korea*

Abstract

This study investigated the catalytic chemisorption of cyanogen chloride(CK) with a metal(ASZM) – triethylenediamine(TEDA) complex. XPS data, IR spectra, and DFT calculations demonstrated that the synergetic catalytic hydrolysis of CK by ASZM-TEDA is kinetically favorable, with the enhanced reactivity of water on the catalyst as the primary cause for the accelerated catalytic hydrolysis. To validate the results, ASZM-TEDA was impregnated into activated carbon beads to form a packed-bed reactor for this breakthrough experiment. The proposed species-transport equation parameters were fitted using the genetic algorithm, and the correlation between parameters was compared. The study concludes that TEDA can affect the diffusivity for overall mass transfer-related reactions and accelerate the catalytic reaction of metal with CK. This study is the first to describe chemisorbed breakthrough with catalyst reaction in-depth and provides insights into the optimized ratio between TEDA and metal complexes. This methodology can be applied to various breakthrough experiments with chemical reactions.

Keywords: Cyanogen Chloride, Chemisorption, Machine Learning, Genetic Algorithm, Breakthrough Curve

1. Introduction

Cyanogen chloride (CK) is a highly volatile and toxic chemical asphyxiant that interferes with the body's ability to use oxygen [1, 2]. It has a low molecular weight, and although pure activated carbon has a high surface area and extended pore network, its contribution alone to removing CK is insufficient. Therefore, the catalytic destruction of CK requires extensive investigations [3]. Useful for military purposes, such as for personal protection gas masks, metal ions impregnated into activated carbon to create active surface sites improve the adsorption ability of CK from the air [2]. Since World War I, activated carbon impregnated with copper and chromium salts, stabilized by an ammonia complex (ASC), have been used. ASC is a well-known and effective adsorbent of CK and hydrogen cyanide [2, 4, 5]. However, as chromium compounds are toxic and have associated environmental regulations, ASC has been replaced with copper, zinc, molybdenum, and silver metals with triethylenediamine (1,4-diazabicyclo[2,2,2] octane, TEDA) complex is impregnated into activated carbon (ASZM-TEDA) [6]. Considering CK adsorption, several papers report copper, zinc salt, and TEDA performs the function of hydrolysis chemical adsorption [2, 4, 6]. However, the specific interactions and synergism of these species are still debated [7]. The TEDA or metal-impregnated activated carbon is also broadly used for hazardous materials adsorption such as NO_2, SO_2 [8], dimethylsulfoxide [9], NH_3 [10], and methyl iodide [11, 12, 13]. It is confirmed that optimum ratios of impregnated carbon can enhance the adsorption capacity with almost irreversible chemical adsorption.

Most adsorption studies are based on physical adsorption (physisorption). A normal breakthrough curve, in which only physisorption occurs, shows a symmetrical curve similar to a sigmoid function [14, 15, 16]. Especially, recent

*Corresponding author
Email address: mkkim@add.re.kr (Min-Kun Kim)
[1] Present address: Department of Chemical and Biomolecular Engineering, University of California, Berkeley, Berkeley, 94720, CA, USA

Abbreviations: Activated carbon impregnated with copper, zinc, silver, molybdenum, and triethlyenediamine (ASZM-TEDA), genetic algorithm (GA), Cyanogen chloride (CK), ASZM-TEDA-impregnated activated carbon beads (ATAB), Brunauer–Emmett–Teller (BET), flame-ionized detector (FID), mass flow controller (MFC), gas chromatograph (GC), natural population analysis (NPA), linear driving force (LDF), density functional theory (DFT)

studies analyzed the symmetrical breakthrough curve using the mass transfer and dispersion effect in the fixed-bed adsorber [17] or Bohart-Adams, Thomas, and Yoon-Nelson model [18, 19, 20] to analyze the kinetics and breakthrough performance inside the reactor. However, for chemical adsorption (chemisorption), relatively few studies describe the reaction mechanism and the breakthrough curve, owing to the complicated reactions involved. Certain studies show the breakthrough curve for the chemisorbed H_2S, which has a slightly different shape than the normal physisorption graph. In particular, the curve shows a flatter curve after the inflection point of the breakthrough curve. In our experiment, the CK breakthrough curve shows a similar curve to that of H_2S. However, previous work on H_2S focused on the position before the inflection point, which does not include the asymmetrical points of the breakthrough curve [21, 22, 23]. Focusing on the impregnated activated carbon, recent studies showed the physical and chemical adsorption mechanisms by analyzing the breakthrough and gas uptake analysis [11, 24]. H_2S chemisorption mechanism through CuO was confirmed using the multiple desulfurization and regeneration steps breakthrough experiments [24]. Also, the chemical adsorption-based removal of methyl iodide was confirmed by analyzing gas uptake and breakthrough performances and applying mass transfer zone fraction to analyze the inflection points in the breakthrough curve [11]. Even though there are several studies describing the chemisorption phenomenon using the breakthrough test, it needs more clear description to understand the gas species transport and breakthrough experiment in the packed-bed system.

In this study, activated carbon beads impregnated with various metal and TEDA combinations were synthesized to perform the breakthrough experiment with a packed-bed reactor. A uniform size of activated carbon beads was selected for numerical analysis. Possible reaction mechanisms were proposed based on the results from X-ray photoelectron spectroscopy (XPS) and infrared (IR) spectroscopy of the initial and the final materials after the reaction with CK and pure ASZM metal and TEDA. To validate the mechanism, the density functional theory (DFT) calculation was performed first, and then the species transport equation for the system was revised, including the reactor reaction, and compared with the resulting breakthrough curve. As CK has limited information about adsorption and reaction properties due to its toxicity, tangibly reasonable physical parameters for the reaction were found using the genetic algorithm (GA). The governing equation must be solved over time to apply a GA. Therefore, by using the Crank–Nicolson finite difference method (FDM) with the tridiagonal matrix algorithm, the partial differential equation for species transport was solved and applied to the GA. Finally, the proposed mechanism was validated using experimental and modeling data. This work is the first to describe the breakthrough curve behavior of chemisorbed materials with catalyst reaction and analyze the mechanism of hydrolysis of CK using the breakthrough curve and species transport phenomena.

2. Experimental

2.1. Synthesis

2.1.1. Reagents

Zinc oxide (ZnO, ≥99.0%), copper(II) carbonate basic ($CuCO_3{\cdot}Cu(OH)_2$, ≥95%), silver nitrate ($AgNO_3$, ≥99.0%), ammonium molybdate tetrahydrate ($(NH_4)_6Mo_7O_{24}{\cdot}4H_2O$, ≥99.0%), ammonium carbonate ($(NH_4)_2CO_3$, ≥30.0% NH_3 basis), ammonia solution 30%, and 4-diazabicyclo[2.2.2]octane (TEDA, ≥99.0%) were purchased from Sigma-Aldrich (St. Louis, MO, USA). Activated carbon beads were purchased from PureSphere (Nonsan, South Korea). All chemicals were used as received without further treatment.

2.1.2. Preparation of metal impregnation solution

For the metal impregnation (ASZM) solution, a mixture of 3.11 g of ZnO, 4.35 g of $CuCO_3{\cdot}Cu(OH)_2$, 0.04 g of $AgNO_3$, 1.84 g of $(NH_4)_6Mo_7O_{24}{\cdot}4H_2O$, and 9.0 g of $(NH_4)_2CO_3$ were dissolved in 15.0 mL of 30% ammonia solution. To lower the viscosity of the solution, up to 100 mL of distilled water was added. The solution was stirred at 25 °C for at least 12 h.

2.1.3. Impregnation of metals and TEDA

Metal-impregnated activated carbon beads (ASZM-AcB) were synthesized using the incipient wetness method. First, approximately 3–5 mL of ASZM impregnation solution was mixed with 1.5 g of activated carbon beads according to the desired concentration. To proceed with uniform impregnation, ASZM solution was added <1 mL at a time and mixed with a spatula. The mixture was then dried in an oven under vacuum at 100 °C for 3 h and 130 °C for 1 h. After cooling the mixture at room temperature, TEDA was mixed with ASZM-AcB and placed in a rotary flask. The flask was placed in a rotary evaporator with a 60 °C water bath and sealed to prevent the sublimation of TEDA. After reacting for 6 h, the sample (ASZM-T-AcB or ATAB) was cooled for 30 min and stored. The naming convention

"ATAB-MMMTT" was used for the various samples in this paper. The first three digits indicate the loaded Cu weight percent relative to carbon weight (MM.M%), and the next two digits indicate the loaded TEDA weight percent relative to carbon weight (TT%). The specific notation of each sample used in this paper is presented in Table S1.

2.2. Characterization

Scanning electron microscopy (SEM) and energy dispersive X-ray spectroscopy (EDS) analysis were performed on a JSM-IT500HR scanning electron microscope (JEOL, Tokyo, Japan) equipped with an Xplore EDS detector (Oxford Instruments, Abingdon, UK) with acceleration voltages ranging from 5 to 10 kV. X-ray photoelectron spectroscopy (XPS) was performed using Nexsa G2 (Thermo Scientific, Waltham, MA, USA). Nitrogen adsorption measurements were performed at 77 K using an ASAP 2020 system (Micromeritics Instrument Corp., Norcross, GA, USA). Before analysis, the samples were degassed at 363 K for 2 h under a vacuum. The nitrogen isotherm data were used to calculate the specific surface area using the Brunauer–Emmett–Teller (BET) method and pore size distribution using the DFT model. The TEDA loading amount was quantified based on the MIL-DTL-32101 extraction method [25]. Each sample was extracted three times with methanol and analyzed by a gas chromatograph with a flame-ionized detector (GC 6850, Agilent Technologies, Madison, WI, USA) [11].

2.3. Breakthrough and pressure drop experiments

A breakthrough experiment with a fixed bed was performed to verify the proposed model for CK adsorption. The schematic diagram of breakthrough experiments is shown in Fig. S1, and the operating conditions are presented in Table S2. The test tube had an inner diameter of 3.9 mm and was temperature-controlled. Materials for the breakthrough experiments were packed to a height of 2 cm. To control the feed concentration and humid condition of CK to 4000 mg/m^3 and RH 80% respectively, 20000 mg/m^3 of CK was diluted with humid nitrogen gas with a ratio of 4 : 1. For testing, a large volume of inlet gas with a vent line was used to control inlet concentration. To protect the liquefaction of humid CK, all tubes were temperature-controlled. A gas chromatograph (GC 7890B, Agilent Technologies, Madison, WI, USA) with a flame-ionized detector (FID) was used to quantify the breakthrough amount of CK. A 6-port valve system was used for injecting outlet gas to the FID detector without disturbing gas flow through the test tube. The 6-port valve system contained one inlet connected to the outlet of the test tube. A volumetric flow rate of 42.3 mL/min was controlled with a mass flow controller (MFC) for outlet flow from the gas chromatograph (GC) valve system. Pressure drop measurements were performed using a differential pressure meter (testo510, Testo, PA, USA) by attaching at the top and bottom of the tube with various bed depths and linear velocities.

2.4. DFT calculation

All the calculations were performed using Gaussian 16 software [26], DFT level of B3LYP (Becke's three-parameter hybrid exchange functional with LYP correlation functional), and the basis set of 6-31++G(d, p) for C, H, O, N, and Cl atoms. The Double-ζ LanL2DZ basis set for Cu was used with the inclusion of effective core potential and associated pseudo-potentials with Grimme correction, which was reported to successfully compute the hydration of $CuCO_3Cu(OH)_2$ complexes [27]. Further, auto-fitting was implemented for the basis sets, and an ultra-fine grid was exploited for two-electron integrals with symmetry being turned off via external command. Geometry optimizations of all reactants and products were performed using the DFT. To ensure that the geometries computed featured minimum energies and to obtain the molecular energies, subsequent harmonic frequency calculations were performed at the same level of theory and using the same basis sets. All potential energies were proven to be global minima after checking that no imaginary frequency was found in the frequency calculations. A natural population analysis (NPA) study was implemented using the NBO 3.1 version, which is included in the Gaussian 16 software.

2.5. Species transport equation

Based on the mole balance and in terms of the molar flux in the 1D system, (W_z) can be written as

$$-\frac{\partial W_z}{\partial z} + r_A = \frac{\partial c}{\partial t} \tag{1}$$

where r_A is the rate of reaction per unit volume, and c is the concentration of species.

Then, the molar flux can be written for a fixed coordinate system, based on Fick's first law, as follows

$$W_z = -D\frac{dc}{dz} + cu \tag{2}$$

where D is the diffusivity and u is the velocity of the species in z direction.

Therefore, the basic form of the reaction–convection–diffusion equation can be derived by substituting the molar flux in the mole balance

$$\frac{\partial c}{\partial t} + u\frac{\partial c}{\partial z} - D\frac{\partial^2 c}{\partial z^2} - r_A = 0 \tag{3}$$

Transport phenomenon due to mass transfer resistance regarding the adsorption rate on the particles can be assumed using the linear driving force (LDF) model [28, 29, 30], and this equation is given by

$$\frac{\partial c}{\partial t} + u\frac{\partial c}{\partial z} - D\frac{\partial^2 c}{\partial z^2} + \left(\frac{1-\epsilon}{\epsilon}\right)\rho_b\frac{\partial \overline{q^*}}{\partial t} - r_A = 0 \tag{4}$$

where ϵ is the bed porosity and $\partial\bar{q}/\partial t = k_{\mathrm{LDF}}(q^* - \overline{q^*})$. k_{LDF} is the mass transfer coefficient based on the LDF model, ρ_b is the bed density, q^* is the adsorbed-phase concentration in equilibrium, and $\overline{q^*}$ is the adsorbed-phase concentration. For the q^*, among various adsorption isotherms, three representative isotherms, Langmuir, Freundlich, and Henry (linear) isotherms, can be used and are written as follows.

$$\begin{aligned} q^* &= q_m\frac{bc}{1+bc} \\ q^* &= K_F c^{1/n} \\ q^* &= K_L c \end{aligned} \tag{5}$$

where q_m is the maximum adsorbed amount in Langmuir isotherm, b is Langmuir isotherm coefficient, K_F is Freundlich isotherm coefficient, n is Freundlich correction factor, and K_L is linear isotherm coefficient. With the bed depth L, boundary conditions for the above mass balance equation are as follows.

$$\begin{aligned} c &= c_0; \quad (z = 0, t > 0) \\ \partial c/\partial z &= 0; \quad (z = L, t > 0) \end{aligned} \tag{6}$$

Initial conditions for the above mass balance equation are given by

$$\begin{aligned} c &= c_0; \quad (z = 0, t = 0) \\ \overline{q^*} &= 0; \quad (0 < z \le L, t = 0) \\ c &= 0; \quad (0 < z \le L, t = 0) \end{aligned} \tag{7}$$

2.6. Non-linear regression using the Genetic Algorithm

To validate the reaction models proposed from the experiment results and find the parameters of the proposed species transport equation, non-linear regression was performed based on the GA between breakthrough experiment data and the solution of a partial differential equation. GA is a revolutionary algorithm inspired by the process of natural selection [31]. GA is a powerful and flexible technique for solving optimization problems, including non-linear large-search space problems [32, 33, 34]. All partial differential equations (PDEs) were substituted using the Crank–Nicolson FDM using the time and location-stepping approach and the tridiagonal matrix algorithm (Thomas algorithm). The rearranged PDEs were then solved using Python [35]. Detailed derivations are provided in Supplementary information.

In this study, to track the effects of the reaction properly, the experimentally controlled conditions (feed concentration, velocity, temperature, and porosity of the packed-bed reactor) were assumed as constant. For the GA setting, the PyGAD library was used [36]. Each PDE solution has a different breakthrough graph trend; thus, the solution of the governing species transport equation as a function of time at the outlet ($c(t)|_{z=L}$) was selected as the regression function. In addition, the squared error between the simulated value ($h(t)$) and experiment value (y_t) at time t was calculated and used as a loss function, and the sum of the weighted loss function was used as a cost function for regression. The breakthrough point is the most important feature; therefore, it is weighted more than the other points.

The cost function was used as a fitting function in the GA. After the parameter estimation, the correlation between parameters was calculated using SPSS Statistics software [37].

$$\text{Regression function} : h(t) = c(t)|_{z=L} \text{ from } \frac{\partial c}{\partial t} + u\frac{\partial c}{\partial z} - D\frac{\partial^2 c}{\partial z^2} + \left(\frac{1-\epsilon}{\epsilon}\right)\rho_b \frac{\partial \overline{q^*}}{\partial t} - r_A = 0$$
$$\text{Loss function} : L(h(t), y_t) = (h(t) - y_t)^2$$
$$\text{Cost function} : J(h) = \sum_{i=0}^{n} \omega_i L(h(t_i), y_i) \tag{8}$$

3. Results and Discussion

3.1. Physical characterization

Fig. S2 shows the activated carbon beads with different size magnitudes. The average diameter of the activated carbon beads was 389.59 ± 15.65 μm. The surface of the activated carbon beads is exceptionally smooth, and the metals and TEDA may not have been evenly impregnated; therefore, to observe the cross-section of the particle after impregnation, the particles were cold-mounted, and SEM-EDS analysis was performed. Fig. S3 shows the SEM-EDS images of the activated carbon beads, ASZM-only-impregnated activated carbon beads, and ASZM-TEDA-impregnated activated carbon beads. EDS mapped data revealed that all metals and TEDA were evenly distributed along the surface and cross-section. In addition, EDS analysis enabled the calculations of the weight percent of each element and are presented in Table S3. ATAB-00000, which is pure activated carbon, contained only carbon and oxygen. ATAB-06000, which the ASZM solution impregnated, contained nitrogen (from ammonium) and metals (copper, zinc, molybdenum, and silver). ATAB-06010, which ASZM and TEDA impregnated, showed a slight increase in the carbon and nitrogen ratio due to TEDA. To see the pore structure of the activated carbon beads, Brunauer-Emmett-Teller (BET) surface area and total pore volume at $P/P_0 = 0.95$ were calculated based on nitrogen adsorption isotherms and pore size distribution analysis (Fig. S4, Table S4). Fig. S4a and S4b show the nitrogen adsorption isotherms at 77K, and Fig. S4c and S4d show the pore size distribution of the samples. The pure activated carbon bead (ATAB-00000) had a BET surface area and total pore volume of 1674.45 m^2/g and 0.81 cm^3/g, respectively. Using the DFT calculation, the activated carbon bead had pores at 0.73 nm, with a broad pore between 1.0 and 4.0 nm. TEDA-only impregnated activated carbon beads, ATAB-00005 and ATAB-00010 showed specific surface areas of 1417.36 and 1327.85 m^2/g with pore volumes of 0.68 and 0.65 cm^3/g, respectively. It shows a small decreasement in surface area with uniformly covered pores. ASZM only impregnated activated carbon beads, ATAB-03000, ATAB-06000, and ATAB-09000 showed specific surface areas of 1140.39, 1112.45, and 1011.91 m^2/g with pore volumes of 0.48, 0.50 and 0.44 cm^3/g, respectively. Compared with TEDA-only impregnated carbon, metal mainly covers the pore over 1.5 nm, and the surface area decreased more. The ASZM-TEDA impregnated activated carbon beads, ATAB-03005, ATAB-06005, ATAB-06010, ATAB-06015, and ATAB-09005 showed specific surface areas of 1040.16, 904.45, 815.88, 627.13, and 903.74 m^2/g with pore volumes of 0.45, 0.41, 0.38, 0.29, and 0.42 cm^3/g, respectively. These results indicate that after the metal and TEDA impregnation, the specific surface area decreased by impregnated molecules covering the micro and meso pores [11].

3.2. Reaction of CK

To analyze the bifunctional effects of ASZM and TEDA-impregnated activated carbon, each component was impregnated and the reaction at each site was analyzed. After analyzing the adsorption properties of each site, both components were impregnated and the bifunctional properties of the ASZM and TEDA-impregnated activated carbon for CK adsorption were analyzed.

3.2.1. Reaction of CK with TEDA

Fig. 1a shows the IR spectra of TEDA before and after the reaction with CK. The peaks at 2750–3500 cm^{-1} were ascribed to the amine group in TEDA. The main differences between the two samples were peaks at 2400–2700 cm^{-1} and 2136 and 2215 cm^{-1}. As shown in Fig. 1c, TEDA can exist in three forms due to protonation in humid conditions[38, 39].

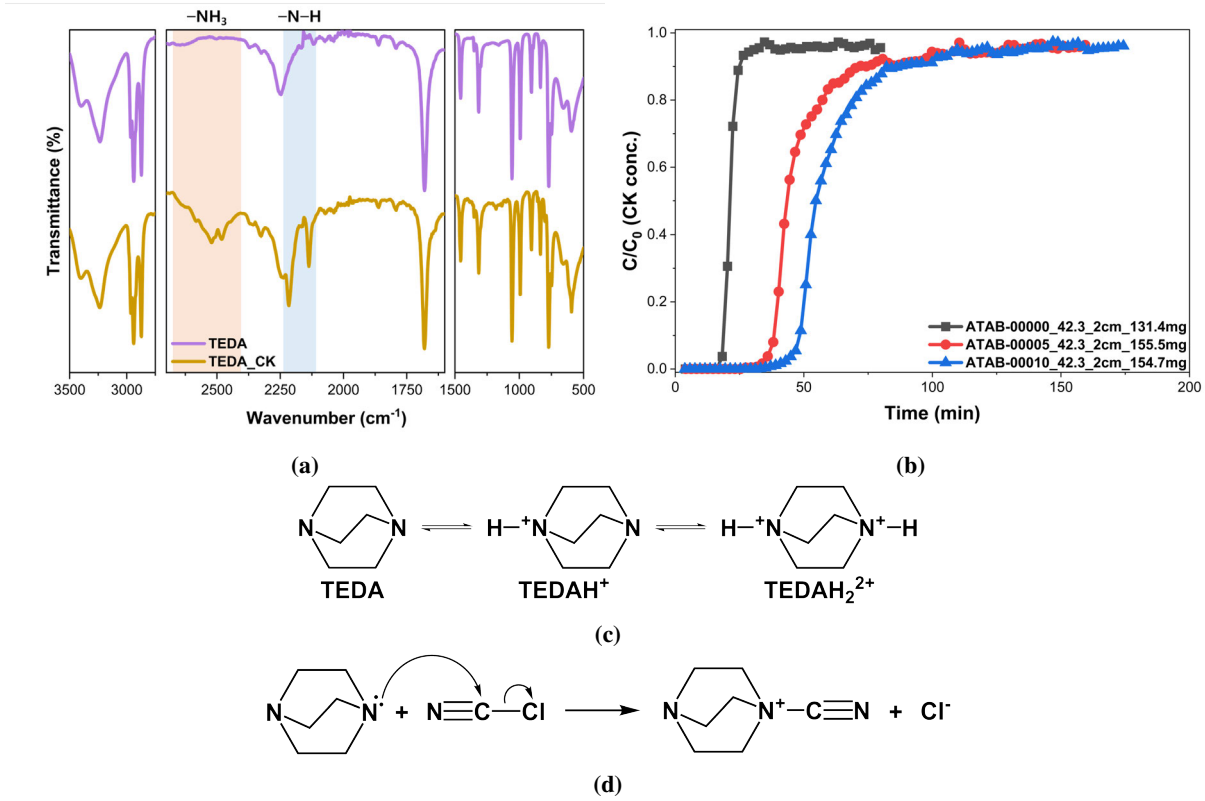

Figure 1: (a) IR spectra of TEDA before and after the reaction with CK; (b) CK breakthrough curve of TEDA impregnated activated carbon; (c) Protonation of TEDA; (d) Reaction between TEDA and CK.

Due to the CK adsorption experiment being performed in humid conditions, the peaks at 2400–2700 cm^{-1} appeared owing to the protonated TEDA. Furthermore, the peaks at 2136 and 2215 cm^{-1} were attributed to $-N-C\equiv N$ vibrational transitions[40]. Therefore, the adsorption of CK on TEDA can be assumed as the following reaction (Fig. 1d) [41, 42].

From the IR spectrum analysis, the possible reaction mechanism between TEDA and CK was determined. To analyze the transport phenomenon, TEDA-impregnated activated carbon beads were used, and the packed-bed-based breakthrough test was performed. Fig. 1b shows the breakthrough curve of TEDA-impregnated activated carbon beads. The reaction stoichiometry between TEDA and CK was calculated based on the breakthrough curve [7].

Table 1: CK breakthrough data for TEDA-impregnated activated carbon beads.

Sample	Mass (mg)	TEDA loading (mmol)	CK adsorption (mmol)	Subtract CK contributions from carbon alone (mmol)
ATAB-00000	131.4	0	0.0576	-
ATAB-00005	155.5	0.066	0.1379	0.0730
ATAB-00010	154.7	0.106	0.1697	0.1077

Table 1 shows that the TEDA-only sample reacted with approximately 1 mol of CK per 1 mol of TEDA. Considering that the reaction between CK and TEDA is chemisorption with a total L_{TEDA} of TEDA sites and that TEDA concentration is represented by $[*]$, the equation for the total number of sites is as follows.

$$L_{\mathrm{TEDA}} = [*] + [\mathrm{CK}*] \tag{9}$$

If the reaction mechanism between CK and TEDA with a reaction rate constant k_{TEDA} satisfies the following equation

$$\mathrm{CNCl} + * \xrightarrow{\mathrm{k_{TEDA}}} \mathrm{CN}* + \mathrm{Cl}^- \tag{10}$$

the reaction rate can be written as

$$\begin{aligned}\frac{d[\mathrm{CNCl}]}{dt} &= -\rho_b k_{\mathrm{TEDA}}[\mathrm{CNCl}][*] \\ &= -\rho_b k_{\mathrm{TEDA}}[\mathrm{CNCl}](L_{\mathrm{TEDA}} - [\mathrm{CN}*])\end{aligned} \tag{11}$$

$$\frac{d[\mathrm{CN}*]}{dt} = k_{\mathrm{TEDA}}[\mathrm{CNCl}](L_{\mathrm{TEDA}} - [\mathrm{CN}*]) \tag{12}$$

Finally, the reaction part of Eq. 4 can be written based on the above TEDA-involved reactions.

$$\begin{aligned}r_{\mathrm{TEDA}} &= -\rho_b k_{\mathrm{TEDA}} c(q^{**} - \overline{q^{**}}) \\ \frac{\partial \overline{q^{**}}}{\partial t} &= k_{\mathrm{TEDA}} c(q^{**} - \overline{q^{**}}) \\ q^{**} &= \text{Total TEDA amount}\end{aligned} \tag{13}$$

with the boundary (Eq. 6) and initial (Eq. 7) conditions. And additional initial condition is $\overline{q^{**}} = 0$ ($0 < z \leq L, t = 0$).

3.2.2. Reaction of CK with metals

Fig. 2a shows the IR spectra of the dried ASZM solution powder before and after the reaction with CK. Commonly, the ammonium from ammonium carbonate absorbs strongly in the range 3100–3300 cm^{-1} owing to antisymmetric and symmetric stretching [43]. The main differences between the two peaks are indicated in Fig. 2a. The broad peak at 2750–3750 cm^{-1} indicates the $-$OH and $-$NH group. C$-$O stretching appeared at 1100 and 1062 cm^{-1} (alkyl cyanates) [43, 44]. Furthermore, the C$-$O$-$H bending peak was observed at 1387 cm^{-1} [43] and the $-$C$\equiv$N peak was observed at 2066 cm^{-1} [45]. Therefore, the IR analysis confirmed the reaction product cyanic acid (HOCN). As presented in Fig. 2c, cyanic acid easily changed to its tautomer isocyanic acid (HNCO), and the $-\,^{-}$N$=$C$=$O peak slightly appeared at 2100–2200 cm^{-1}. Furthermore, the peak for the N$-$H bend at 1619 cm^{-1} also increased after the reaction with CK.

To observe the chemical reaction between the ASZM solution and CK, XPS analysis was performed. The wide-scan survey XPS spectra show that ASZM powder included the basic metals and solvent, and CK-reacted ASZM powder adsorbed some chlorine from CK (Fig. S5a). Within the XPS data, Cu 2p, Zn 2p, and C 1s indicate that the XPS spectra were very similar before and after the reaction. The convolution of Cl $2p_{3/2}$ (197.9 eV) and $2p_{1/2}$ (199.5 eV) shown in Fig. 2d, indicate that chlorine was chemically bonded with the dried ASZM solution as NH_4Cl [46]. Fig. S5b shows the convolution of Cu $2p_{3/2}$ XPS spectrum. The XPS peak of ASZM and ASZM-CK at 932.6 eV indicate Cu/Zn composite [47]; thus, the peak for $Cu(OH)_2$ was observed at 934.2 eV [48] and the peak for $CuCO_3$ was observed at 935.1 eV [49]. Fig. 2e shows the convolution of N 1s XPS spectrum. The peak at 396.4 eV was assigned to N$-$Mo bonding [50, 51], and the peak at 397.4 eV denoted a nitrogen interaction with metal [49]. The peak for C$-$$NH_2$ was observed at 399.3 eV [52], and the ammonium ion appeared at 401.5 eV [53]. For CK-adsorbed ASZM samples, the peaks for N$-$Mo bonding and N$-$metal bonding decreased, and a peak at 397.6 eV was observed, indicating the presence of cyanide compounds [54]. Fig. 2f shows the O 1s XPS spectrum. The peaks at 530.0, 531.1, 531.7, and 533 eV are assigned to ZnO, C$-$O, $Cu(OH)_2$, and C$=$O (from $CuCO_3$), respectively [55]. As seen from the spectrum, the peak for ZnO significantly decreased, and the peak for C$-$O increased, indicating cyanic acid formation. Fig. S5c shows the XPS spectrum of Zn. The peaks at 1021.3, 1021.6, and 1022.1 eV indicate the Zn$-$N (from metal and ammonium interaction), Cu/Zn composite, and Zn$-$O, respectively [47, 56]. The peak decrease in both oxygen and zinc XPS spectra suggests that Zn^{2+} acted as an oxidizing agent and co-catalyst with Cu^{2+} [4, 57]. C 1s XPS (Fig. S5d) showed a C$-$C peak at 284.3 eV, C$-$O peak at 285.3 eV, and C$=$O peak at 289 eV [58]. After the CK adsorption, an additional C$\equiv$N peak was observed at 287.3 eV [59]. Mo 3d XPS (Fig. S5e) did not show significant peak changes. Molybdenum functions to increase HCN residence times under humid conditions and does not participate in the reaction with CK [4].

Combining IR and XPS data, if the reaction between CK and metals is a catalytic reaction and the non-volatile product HOCN is formed, the reactions can be written as follows [57].

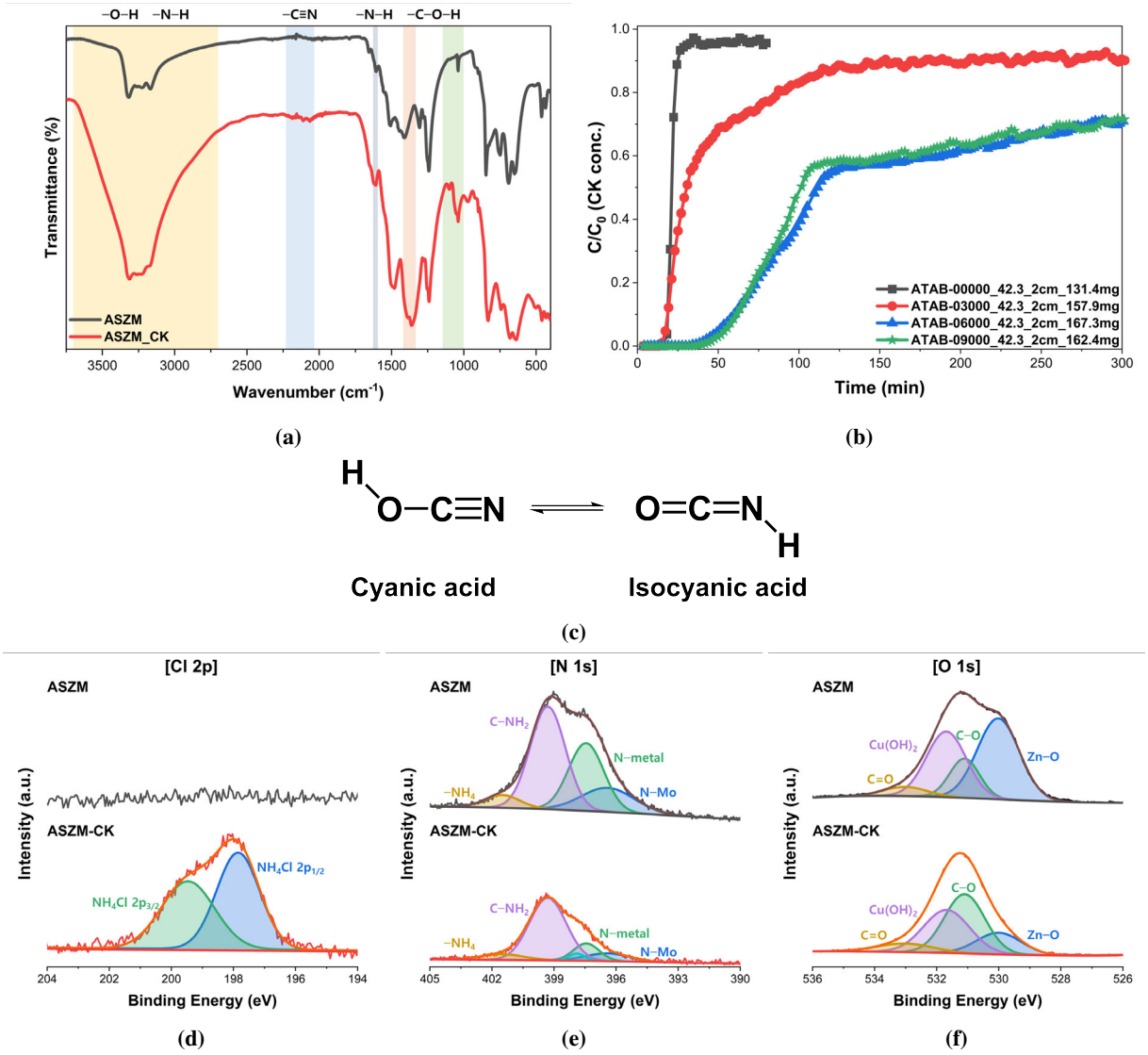

Figure 2: (a) IR spectra of the dried ASZM solution powder before and after the reaction with CK; (b) CK breakthrough curve of ASZM-impregnated activated carbon beads; (c) Cyanic acid and its tautomer isocyanic acid; (d)–(f) XPS data of the dried ASZM solution powder before and after the reaction with CK.

$$
\begin{aligned}
\mathrm{CNCl} &\xrightarrow[\text{Metals}]{\mathrm{H_2O}} \mathrm{HOCN} + \mathrm{HCl} \\
2\,\mathrm{HCl} + (\mathrm{NH_4})_2\mathrm{CO_3} &\longrightarrow 2\,\mathrm{NH_4Cl} + \mathrm{H_2CO_3} \\
\mathrm{H_2CO_3} &\longrightarrow \mathrm{CO_2} + \mathrm{H_2O}
\end{aligned} \tag{14}
$$

The IR and XPS spectrum analysis determined the possible reaction mechanism between ASZM and CK. ASZM impregnated activated carbon beads were used to analyze the transport phenomenon, and the packed-bed-based breakthrough test was performed. Fig. 2b shows the breakthrough curve of ASZM–impregnated activated carbon beads with different impregnation ratios. At low concentrations of ASZM solution, the breakthrough point was similar to that of pure activated carbon beads. After the breakthrough point, the curve feature differed from the reference and indicated the extra reaction with CK. When the ASZM concentration increased after the breakthrough point, it followed the standard breakthrough curve with a sigmoid-like graph. However, after reaching a certain point, when the

outlet concentration had not yet reached inlet concentration and saturation occurred, the outlet concentration slightly and linearly increased. Furthermore, the breakthrough points and curves were similar if the ASZM concentration was higher than a certain number. The results indicate that the reaction between CK and ASZM solution was catalytic, confirming the previously written reaction mechanism. Based on the proposed mechanism, the rate expression is written as follows for separable deactivation kinetics, assuming a second-order decay with a decay rate constant k_d and time-dependent activity coefficient $a(t)$.

$$-r_{\text{metal}} = \rho_b k_{\text{metal}} a(t) c \tag{15}$$

$$r_d = -\frac{da}{dt} = k_d a(t)^2 \tag{16}$$

Therefore, the reaction part of Eq. 4 can be written based on the above ASZM-involved reactions.

$$\begin{aligned} r_{\text{metal}} &= -\rho_b k_{\text{metal}} a(t) c \\ -\frac{da(t)}{dt} &= k_d a(t)^2 \end{aligned} \tag{17}$$

with the boundary (Eq. 6) and initial (Eq. 7) conditions. And additional boundary condition is $a(t) = 1$ ($z > ut$).

3.2.3. Reaction of CK with metals and TEDA

Fig. 3a shows the IR spectrum of the TEDA–impregnated dried ASZM solution powder before and after the reaction with CK. After the reaction with CK, the main differences between the peaks are highlighted in Fig. 3a. Due to TEDA and CK interaction, the peaks at 2058 and 2210 cm^{-1} were attributed to $-N-C\equiv N$ vibrational transitions. Due to ASZM solution and CK interaction, peaks at 1062, 1287, and 1619 cm^{-1} were attributed to alkyl cyanates, $C-O-H$, and $N-H$ bend, respectively. The peaks at 3100–3300 and 3551 cm^{-1} were assigned to $-OH$ bonds, which appeared more significantly compared with that of the TEDA or ASZM–only impregnated carbon.

XPS analysis was performed to discover the reaction between TEDA–impregnated dried ASZM solution and CK. Fig. S6a shows the wide-scan XPS survey spectrum. Compared with the reaction of CK with ASZM, most of the elements show similar results. Fig. 3b shows the spectrum of Cl 2p, which similarly deconvoluted to 197.9 and 199.5 eV, indicating NH_4Cl [46]. For Cu 2p, all peaks shifted approximately 0.1 eV compared to the CK reaction with ASZM due to TEDA impregnation (Fig. 3c). Peaks were attributed to Cu/Zn composite, $Cu(OH)_2$, and $CuCO_3$ at 932.7, 934.3, and 935.2 eV, respectively [47, 48, 49]. Similar to that of Cu 2p, the N 1s peaks shifted approximately 0.1 eV compared to the CK reaction with ASZM (Fig. 3d). The peak for N-Mo bonding was observed at 396.5 eV [50, 51], N-metal at 397.6 eV [49], $C-NH_2$ at 399.5 eV [52], ammonium ion at 401.6 eV [53], and $-NR_3$ corresponding to TEDA at 402 eV [60]. After the CK reaction, the nitrogen and metal bonding peak decreased, and both the cyanide compound peak at 397.6 eV and $-NR_3$ peak at 402 eV significantly increased. These results indicate that a reaction occurred between TEDA and CK. Fig. S6b shows the O 1s XPS spectrum. The oxygen peak also shifted 0.1 eV compared to that of the dried ASZM solution powder case. The peaks at 530.1, 531.2, 531.8, and 533.1 eV were assigned to ZnO, $C-O$, $Cu(OH)_2$, and $C=O$ (from $CuCO_3$), respectively [55]. Fig. S6c shows the Zn 2p XPS spectrum. All peaks were shifted slightly compared to that of the CK reaction with ASZM. The peaks at 1021.4, 1021.8, and 1022.2 eV indicate $Zn-N$, Cu/Zn composite, and $Zn-O$ [47, 56]. Similar to that of the reaction between ASZM and CK, the oxygen and zinc XPS peaks of ZnO showed that Zn^{2+} reduced to Zn [4, 57]. C 1s XPS (Fig. S6d) shows the $C-C$, $C-O$, and $C=O$ peaks at 284.3, 285.3, and 289 eV, respectively [58]. Furthermore, due to TEDA, the $C-N$ peak at 286.6 eV was observed [58]. After the CK adsorption, similar to that of the ASZM reaction with CK, an additional $C\equiv N$ peak appeared at 287.3 eV [59]. In addition, similar to that of the ASZM-only reaction with CK, Mo 3d XPS (Fig. S6e) did not show significant peak changes.

The IR and XPS analysis show the possible reaction between ASZM-TEDA and CK. ASZM and TEDA were impregnated with activated carbon beads for more precise analysis, and the breakthrough test was performed. Fig. 3e and 3f show the breakthrough curves of ASZM and TEDA-impregnated activated carbon beads with different impregnation ratios. Compared to that of TEDA-only or ASZM-only impregnated activated carbons, the breakthrough point shifted significantly, indicating that ASZM and TEDA have bifunctional reactions with CK. The nitrogen atom in TEDA interacted with water owing to its hydrophilic characteristic [61], indicating that TEDA retained the water ligand from the metal ion complex [57], which helped the metal act as a catalyst for the hydrolysis of CK. Similar

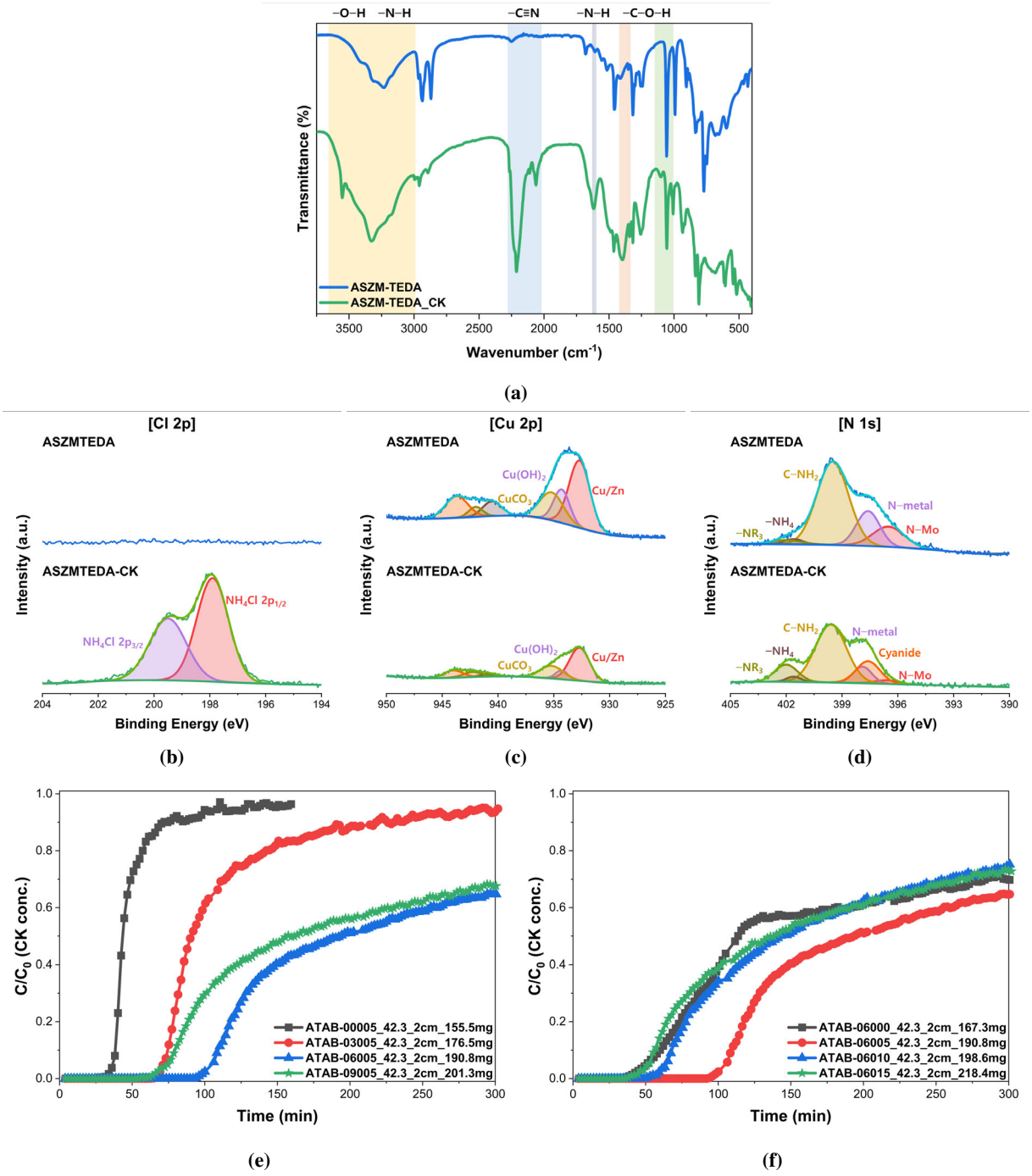

Figure 3: (a) IR spectra of the TEDA-impregnated dried ASZM solution powder before and after the reaction with CK; (b) –(d) XPS data of the TEDA-impregnated dried ASZM solution powder before and after the reaction with CK; CK breakthrough curve of ASZM and TEDA-impregnated activated carbon with different (e) ASZM; (f) TEDA ratio.

to that of the ASZM-only-impregnated activated carbon breakthrough curve in Fig. 2b, deactivation kinetics for the catalyst reaction were observed.

Based on the TEDA-only and ASZM-only reactions (Eq.13 and 17), the overall species transport equation for the ASZM and TEDA-impregnated activated carbon can be written as

$$\frac{\partial c}{\partial t} + u\frac{\partial c}{\partial z} - D\frac{\partial^2 c}{\partial z^2} + \left(\frac{1-\epsilon}{\epsilon}\right)\rho_b \frac{\partial \overline{q^*}}{\partial t} + \rho_b k_{\mathrm{TEDA}} c(q^{**} - \overline{q^{**}}) + \rho_b k_{\mathrm{metal}} a(t) c = 0 \tag{18}$$

with the boundary and initial conditions as follows.

$$\begin{aligned} c &= c_0 \quad (z = 0, t \geq 0) \\ \partial c/\partial z &= 0 \quad (z = L, t > 0) \\ a &= 1 \quad (z > ut) \end{aligned} \tag{19}$$

$$\begin{aligned} \overline{q^*} &= 0 \quad (0 < z \leq L, t = 0) \\ \overline{q^{**}} &= 0 \quad (0 < z \leq L, t = 0) \\ c &= 0 \quad (0 < z \leq L, t = 0) \end{aligned} \tag{20}$$

3.3. Simulation and numerical modeling

3.3.1. DFT calculation

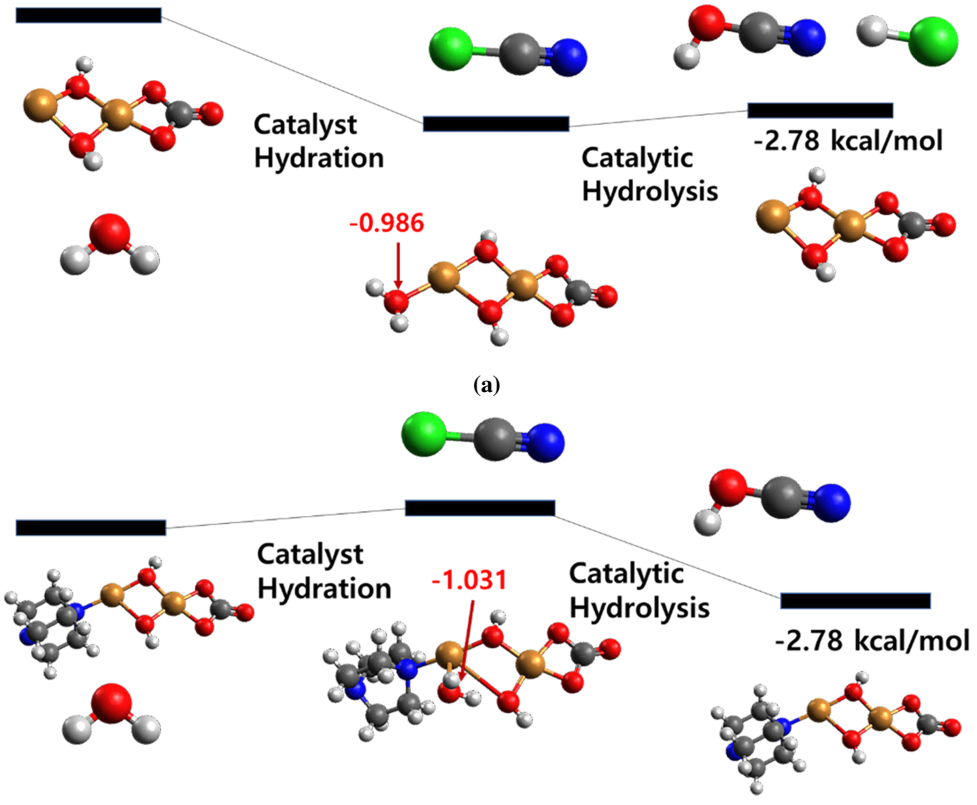

Figure 4: Hydrolysis reaction energy coordinates on CK by two different Cu(II) complexes. Red arrows with red-colored numbers indicate the NPA charges. (a) Hydrated $CuCO_3Cu(OH)_2$; (b) Hydrated $CuCO_3Cu(OH)_2$-TEDA.

To demonstrate the synergetic catalytic hydrolysis of CK by ASZM–TEDA, an investigation was conducted into the energetic reaction mechanism stemming from the copper complex predominantly deposited on the activated carbon surface. $CuCO_3Cu(OH)_2$, which was employed in this study, and its supplementary coordination with a single water molecule has been recently and successfully simulated using DFT [27]. The coordinated water molecule on the $CuCO_3Cu(OH)_2$ complex was simulated, and its energy was subsequently calculated. Moreover, the hydrolysis

reaction of CK by the coordinated water (activated nucleophile) was simulated, revealing an exothermic energy of 2.78 kcal/mol (Fig. 4a), which implied a facile forward reaction and corroborated the experimental findings.

Additionally, TEDA was incorporated into the $CuCO_3Cu(OH)_2$ complex, yielding analogous energy efficiency (Fig. 4b). Upon examining the reaction mechanism for both cases, the hydrolysis reaction was determined to be more facile when originating from the $CuCO_3Cu(OH)_2$-TEDA complex. Furthermore, water complexation is crucial for the accelerated hydrolysis reaction deriving from $CuCO_3Cu(OH)_2$-TEDA. The hydrolysis reaction facilitated by $CuCO_3Cu(OH)_2$-TEDA was kinetically more favorable than that for the catalytic process. Consequently, supplementary calculations and analyses utilizing natural population analysis were performed.

Notably, the larger negative value (indicated by red-colored numbers, –1.031 vs. –0.986 in Fig. 4) on the oxygen atom in water within the $CuCO_3Cu(OH)_2$–TEDA complex provides a successful explanation for the enhanced reactivity of water on the catalyst due to the additional complexation of TEDA. This ultimately substantiates the primary reason for the accelerated catalytic hydrolysis of CK by ASZM-TEDA.

3.3.2. Species transport equation modeling

The breakthrough data were fitted using the GA based on the governing equation proposed with the experimental data. Before the simulation, pressure drop measurement with different linear velocities and packed bed depths was performed. And the Ergun equation (Eq. 21) was used for calculating the bed porosity [62, 63, 64].

$$-\frac{\Delta p}{L} = \frac{150\mu L}{D_p^2}\frac{(1-\epsilon)^2}{\epsilon^3}u + \frac{1.75L\rho_g}{D_p}\frac{(1-\epsilon)}{\epsilon^3}u^2 \tag{21}$$

where Δp is the pressure drop, L is the bed depth, μ is the viscosity of the gas, ρ_g is the density of the gas, D_p is the particle diameter, ϵ is the porosity and u is the velocity of the gas in z direction. Based on the pressure drop measurement results (Table S5) and physical characterization results, $\epsilon = 0.39$ was calculated and used for the packed bed porosity. Feed concentration was $4g/m^3$, and the linear velocity was $5.9cm/s$ based on the experiment setup (Table S2). As GA is a population-based method [65] and the initial range can affect the final results, numerical settings for each parameter was first determined based on the previous studies and books [22, 64, 66]. The range for diffusivity was $0 \sim 10^{-4}$, all rate constant were $10^{-6} \sim 10^{-2}$, isotherm coefficient was $10^0 \sim 10^3$, and maximum chemisorption site was $10^0 \sim 10^1$. To obtain better results, all parameters (ξ) were first divided into the float number (α) range between 1 and 9.99, and the integer exponent term (β) with the base 10 (i.e., $\xi = \alpha \times 10^{\beta}$). Therefore, each parameter needed two solutions, and the algorithm found both solutions to create a parameter. Especially, as all of the samples for the breakthrough test have different densities (Table S6), new value $k' = \rho_b k$ was used for the reaction rate coefficient in simulation. After the fitting, the value is divided by the density to find the k. After finishing each cycle, the range of the integer exponent term was narrowed to more accurately represent information obtained from the simulation. The sum of squares regression, total, and error of each data point was calculated and used as a fitness function. Each dataset was fitted with this process with over 2000 generations and performed over 50 cycles.

Fig. 5 shows the fitted breakthrough curve overlapped with experiment results, and Table S7 shows the parameters estimated based on the GA used for the curve fitting. Fig. 5 presents the dataset and simulation results, which show very similar curve features. From the proposed species transport equation for each reaction (Eq. 13, 17, and 18), the diffusivity term remained because it was not determined if diffusive flux was negligible or not. However, after several cycles of GA, the diffusivity coefficient for ASZM-only impregnated carbon was approximately 10^{-20}. Therefore, the diffusivity term was ignored for ASZM-only impregnated carbon simulations. Also, if the final results of diffusivity show less than 10^{-9}, the values were approximated to 0. To analyze the contribution of each component for CK adsorption, scaling analysis [64, 67] was additionally performed based on the simulation result.

Table 2: Scaling analysis of various CK breakthrough experiment

CK reaction	$\frac{\partial c}{\partial t}$	$u\frac{\partial c}{\partial z}$	$D\frac{\partial^2 c}{\partial z^2}$	$\left(\frac{1-\epsilon}{\epsilon}\right)\rho_p\frac{\partial \overline{q^*}}{\partial t}$	$\frac{\partial \overline{q^{**}}}{\partial t}$	$k_{\text{metal}}a(t)c$
pure carbon	$\sim O(10^{-6})$	$\sim O(10^{-3})$	~ 0	$\sim O(10^{0})$	-	-
TEDA only	$\sim O(10^{-6})$	$\sim O(10^{-3})$	$\sim O(10^{-5})$	$\sim O(10^{-1})$	$\sim O(10^{0})$	-
metal only	$\sim O(10^{-6})$	$\sim O(10^{-3})$	~ 0	$\sim O(10^{-1})$	-	$\sim O(10^{-2})$
metal and TEDA	$\sim O(10^{-6})$	$\sim O(10^{-3})$	~ 0–$O(10^{-6})$	$\sim O(10^{-1})$	$\sim O(10^{-1})$	$\sim O(10^{-1} - 10^{0})$

Table 2 shows the order of magnitude of each component with respect to CK reaction materials. Compared with

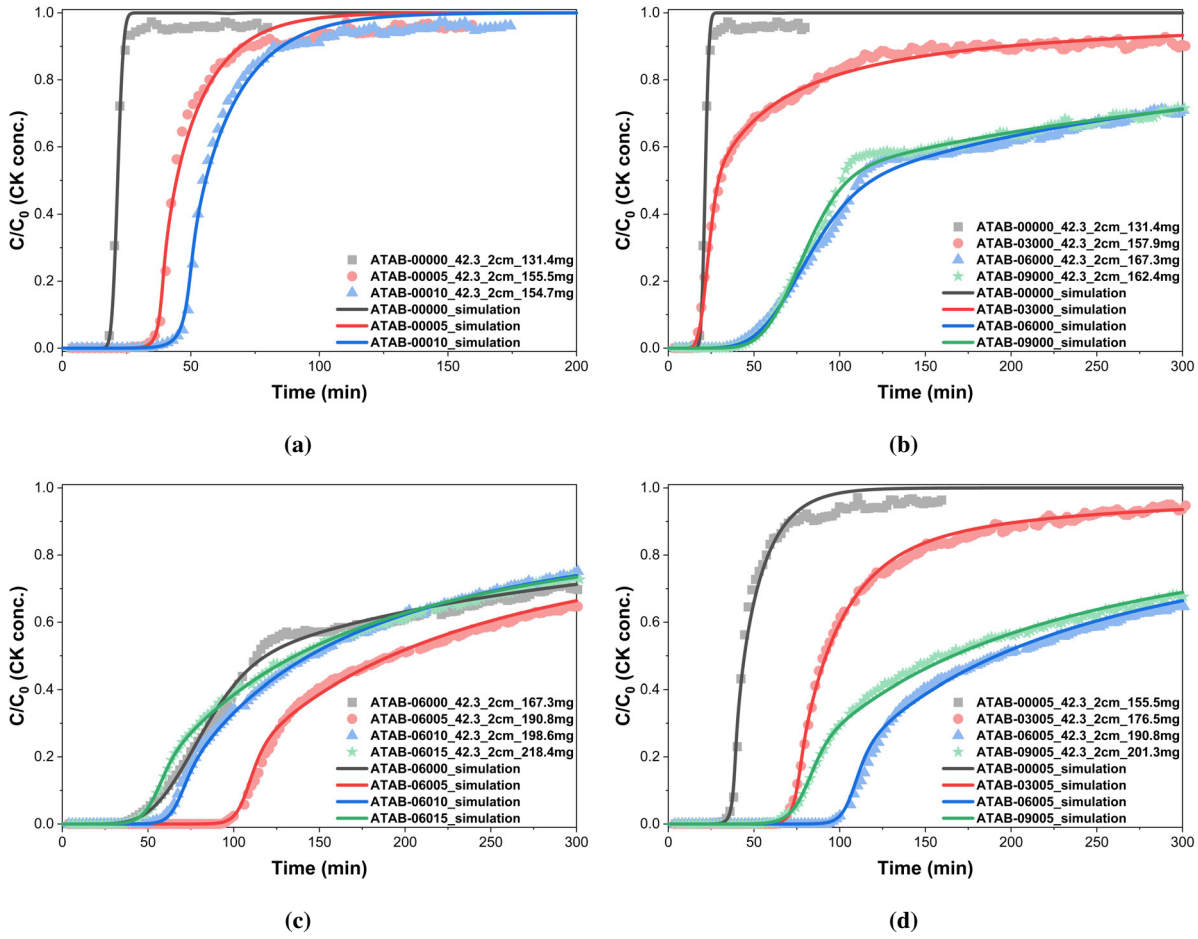

Figure 5: Fitted data based on the proposed reaction of CK with (a) TEDA; (b) ASZM solution; (c)–(d) ASZM-TEDA-impregnated activated carbon beads.

reaction terms and other terms, the scaling analysis confirmed that the reaction terms are dominant in CK adsorption. In the pure carbon case, the physisorption term was dominant. Whenever TEDA is added, CK chemisorption on TEDA is relatively dominant for CK adsorption. As Fig. 1b shows, the breakthrough time for pure carbon was around 18 min, but the existence of TEDA increased the breakthrough time to 27 min (ATAB-00005) and 33 min (ATAB-00010). However, when metal is added, the metal decreases the LDF parameters and slightly increases breakthrough performance due to metal catalytic reaction. As Fig. 2b shows, the breakthrough time slightly increases when the metal is impregnated. Significantly, after the breakthrough, the curve shows a second slope, which is mainly affected by catalytic decay. When decay term (k_d) is not applied, as Fig. S7a shows, catalytic reaction decomposes CK and saturation point changes. However, when catalytic deactivation is applied, the breakthrough curve shows an extra slope which also can be observed in experimental results. In the case when both metal and TEDA are impregnated to carbon, with a small amount, it does not show a significant difference, and each reaction term shows a similar contribution ($\sim O(10^{-1})$) for CK breakthrough (ATAB-03005). But when more metal is impregnated, the order-of-magnitude of catalytic reaction term increased ($\sim O(10^{0})$) with TEDA chemisorption term decreased ($\sim O(10^{-2})$). This also indicated that TEDA accelerates the catalytic hydrolysis of CK by the ASZM-TEDA complex. To see the contribution of each reaction term to the breakthrough curve, additional analysis was performed using the ATAB-06005 simulation result (Fig. S7b). Only the LDF term, mainly a physical adsorption term, shows a typical physical adsorption breakthrough curve with symmetric features. When the TEDA term was applied, the breakthrough time shifted, and as the TEDA reaction site was continuously blocked over time, it reached to LDF breakthrough curve. When the metal term was applied, the breakthrough time slightly shifted, and because of the deactivation term discussed in Fig. S7a, the second slope can be observed in the breakthrough curve. Finally, when both metal and TEDA reaction terms were

applied to the simulation, it shifted more breakthrough time with the other slope. These experimental and simulation results confirm that chemisorption with TEDA shifts the breakthrough time, and catalytic chemisorption with metal affects the slope after the breakthrough. But as there is a limited surface that can cover with metal and TEDA, it has an optimized ratio to obtain the best performance.

To clarify the monotonic relationship between two variables, Spearman's ρ correlation was applied. Table S8 shows the correlations between parameters results from the SPSS Statistics software. As shown in Table S7 and S8, the most significant feature is the diffusivity coefficient (D). The diffusivity coefficient increased as the TEDA active site (q^{**}) increased, implying that the reaction with TEDA is more likely diffusion-dominated, and the reaction with metal is more likely convection-dominated. From the correlation between the mass diffusivity (D) and TEDA reaction coefficient (k_{TEDA}), the TEDA reaction with CK was also relevant to mass transfer-based reactions. Focusing on the TEDA and metal reaction, the co-existence of TEDA and metal decreased the TEDA reaction but increased the metal reaction with CK. This result indicates that the function of TEDA converts from CK adsorption to supporting the CK reaction with metal by binding the water molecules. Lastly, the high correlation between the TEDA reaction site (q^{**}) with the metal reaction coefficient (k_{metal}) and the deactivation coefficient (k_{TEDA}) implies that TEDA highly affects the reaction of CK with the metal complex. With the DFT results (Fig. 4) and correlation results (Table S8), it is obvious that in the presence of water, metal complex, and TEDA have a synergic effect on reaction with CK.

4. Conclusions

In this study, the chemisorption of cyanogen chloride (CK) with an ASZM metal and TEDA complex was analyzed. Before and after each catalytic powder reaction with CK, the XPS and IR spectra were observed and possible reaction mechanisms were derived. From the spectral data, CK directly reacted with TEDA to form TEDA-CN and with a metal present, the metal acted as a water catalyst to convert CK to cyanic acid. To validate these mechanisms, DFT calculation was performed. The synergetic catalytic hydrolysis of CK by ASZM-TEDA was demonstrated through an investigation into the energetic reaction mechanism of the $CuCO_3Cu(OH)_2$-TEDA complex. The hydrolysis reaction facilitated by $CuCO_3Cu(OH)_2$-TEDA was found to be kinetically more favorable, with the enhanced reactivity of water on the catalyst due to the additional complexation of TEDA, which was the primary cause for the accelerated catalytic hydrolysis. For further applications, such as in gas masks, and to validate the previous results, ASZM and TEDA were impregnated into activated carbon beads. These impregnated activated carbon beads were packed into a tube to form a packed-bed reactor for a breakthrough experiment. Derived mechanisms were applied to the reaction–convection–diffusion-based species transport equation, and the solution was compared with the result from the breakthrough experiment. Non-linear regression was performed using the GA, and the correlation between parameters was compared using the SPSS software. The numerical modeling and overall experiment data imply that TEDA can affect the diffusivity for the overall mass transfer-related reaction. Furthermore, TEDA can accelerate the catalytic reaction of metal with CK by forming the water complex; however, the deactivation rate of the catalyst reaction of metal is also affected. With this work, the optimized ratio between TEDA and ASZM–metal complexes for gas masks can be easily obtained. Furthermore, as this work is the first to analyze chemisorbed breakthrough behavior in depth, this methodology can be applied to various breakthrough experiments with chemical reactions.

Nomenclature

$a(t)$	: time-dependent catalytic activity
b	: Langmuir isotherm coefficient ($m^3 \cdot kg^{-1}$)
c	: gas concentration ($kg \cdot m^{-3}$)
D	: diffusivity ($m^2 \cdot s^{-1}$)
D_p	: particle diameter (m)
ϵ	: bed porosity
k	: rate constant (s^{-1})
k_d	: catalyst deactivation constant (s^{-1})
K_F	: Freundlich isotherm coefficient ($kg^{1-1/n}m^{3/n} \cdot kg^{-1}$)
K_L	: Linear isotherm coefficient ($m^3 \cdot kg^{-1}$)
k_{LDF}	: LDF model mass transfer coefficient (s^{-1})
k_{metal}	: CK and metal reaction rate constant ($m^3 \cdot g^{-1}s^{-1}$)
k_{TEDA}	: CK and TEDA reaction rate constant ($m^3 \cdot g^{-1}s^{-1}$)
L	: bed depth (m)
L_{TEDA}	: total TEDA sites ($g \cdot kg^{-1}$)
μ	: viscosity of the gas ($Pa \cdot s$)
n	: Freundlich correction factor
Δp	: pressure drop in packed bed (Pa)
q^*	: maximum physisorbed amount on the bed per unit mass ($kg \cdot kg^{-1}$)
$\overline{q^*}$	: physisorbed amount on the bed per unit mass ($kg \cdot kg^{-1}$)
q^{**}	: maximum chemisorbed amount on the bed per unit mass ($g \cdot kg^{-1}$)
$\overline{q^{**}}$	: chemisorbed amount loading on the bed per unit mass ($g \cdot kg^{-1}$)
q_m	: maximum adsorbed amount in equilibrium
ρ_b	: bed density ($kg \cdot m^{-3}$)
ρ_g	: density of the gas ($kg \cdot m^{-3}$)
r_A	: reaction rate of species A ($kg \cdot m^{-3}s^{-1}$)
r_d	: catalyst deactivation reaction rate (s^{-1})
r_{TEDA}	: reaction rate of CK and TEDA reaction ($kg \cdot m^{-3}s^{-1}$)
r_{metal}	: reaction rate of CK and metal reaction ($kg \cdot m^{-3}s^{-1}$)
u	: linear velocity ($m \cdot s^{-1}$)
W_z	: molar flux ($kg \cdot m^{-2}s^{-1}$)

CRediT authorship contribution statement

Jaeheon Lee: Methodology, Conceptualization, Investigation, Data Collection and Processing (Experimental, Computational), Formal Analysis, Writing -original draft. **Jaekyung Bae:** Data Collection and Processing (Experimental). **Junemo Koo:** Methodology (Computational), Investigation. **Keunhong Jeong:** Data Collection and Processing (Computational). **Sang Myeon Lee:** Formal Analysis. **Heesoo Jung:** Formal Analysis, Funding. **Min-Kun Kim:** Supervision, Conceptualization, Discussion, Writing – review & editing.

Declaration of Competing Interest

The authors declare that they have no known competing financial interests or personal relationships that could have appeared to influence the work reported in this paper.

Data Availability

Data will be made available on request.

Acknowledgement

The authors gratefully acknowledge the Republic of Korea CBR Defense Command for providing CK. We also thank KARA (KAIST Analysis Center for Research Advancement) for assistance with the XPS analysis. This work was supported by the Agency for Defense Development [No. 912751201]

Appendix A. Supporting information

Supplementary data associated with this article can be found in the online version.

References

[1] D. H. Blakey, M. Lafontaine, J. Lavigne, D. Sokolowski, J.-M. Philippe, J.-M. Sapori, W. Biederbick, R. Horre, W. B. Marzi, H. Kondo, et al., A screening tool to prioritize public health risk associated with accidental or deliberate release of chemicals into the atmosphere, BMC Public Health 13 (1) (2013) 1–10. doi:https://doi.org/10.1186/1471-2458-13-253.

[2] A. A. Gorzkowska-Sobas, K. M. Bjørgo, Adsorption performance of activated carbon towards toxic industrial chemicals, Norwegian Defence Research Establishment (2015).
URL `http://hdl.handle.net/20.500.12242/1120`

[3] S. K. Agarwal, J. J. Spivey, D. E. Tevault, Kinetics of the catalytic destruction of cyanogen chloride, Appl. Catal. B-Environ. 5 (4) (1995) 389–403. doi:https://doi.org/10.1016/0926-3373(94)00051-4.

[4] P. Lodewyckx, Chapter 10 Adsorption of chemical warfare agents, in: T. J. Bandosz (Ed.), Activated Carbon Surfaces in Environmental Remediation, Vol. 7 of Interface Science and Technology, Elsevier, 2006, pp. 475–528. doi:https://doi.org/10.1016/S1573-4285(06)80019-0.

[5] Z. Barnir, C. Aharoni, Adsorption of cyanogen chloride on impregnated active carbon, Carbon 13 (5) (1975) 363–366. doi:https://doi.org/10.1016/0008-6223(75)90003-2.

[6] G. Earnest, M. Gressel, R. Mickelsen, E. Moyer, L. Reed, C. Karwacki, R. Morrison, D. Tevault, W. Delp, A. Persily, Guidance for Filtration and Air-Cleaning Systems to Protect Building Environments from Airborne Chemical, Biological, or Radiological Attacks, Cincinnati, Ohio: National Institute for Occupational Safety and Health (NIOSH) (2003).
URL `https://www.cdc.gov/niosh/docs/2003-136/default.html`

[7] J. J. Mahle, G. W. Peterson, B. J. Schindler, P. B. Smith, J. A. Rossin, G. W. Wagner, Role of TEDA as an Activated Carbon Impregnant for the Removal of Cyanogen Chloride from Air Streams: Synergistic Effect with Cu(II), J. Phys. Chem. C 114 (47) (2010) 20083–20090. doi:10.1021/jp106730j.

[8] S. S. Kiani, A. Farooq, Y. Faiz, A. Shah, M. Ahmad, N. Irfan, M. Iqbal, A. B. Usman, A. Mahmood, M. Nawaz, S. Bibi, A. Aziz, Investigation of Cu/Zn/Ag/Mo-based impregnated activated carbon for the removal of toxic gases, synthesized in aqueous media, Diam. Relat. Mater. 111 (2021) 108179. doi:https://doi.org/10.1016/j.diamond.2020.108179.

[9] R. Dhawan, M. Goyal, K. Bhasin, Influence of metal impregnants on adsorption of dimethylsulfide vapors by activated carbons, Mater. Today: Proc. 4 (9) (2017) 10515–10519, international Conference on Recent Trends in Engineering and Material Sciences (ICEMS-2016), March 17-19, 2016, Jaipur, India. doi:https://doi.org/10.1016/j.matpr.2017.06.411.

[10] J. V. Romero, J. W. H. Smith, B. M. Sullivan, L. Macdonald, L. M. Croll, J. R. Dahn, Evaluation of the SO_2 and NH_3 Gas Adsorption Properties of CuO/ZnO/Mn_3O_4 and CuO/ZnO/NiO Ternary Impregnated Activated Carbon Using Combinatorial Materials Science Methods, ACS Comb. Sci. 15 (2) (2013) 101–110. doi:10.1021/co3001132.

[11] K. Ho, S. Moon, H. C. Lee, Y. K. Hwang, C.-H. Lee, Adsorptive removal of gaseous methyl iodide by triethylenediamine (teda)-metal impregnated activated carbons under humid conditions, J. Hazard. Mater. 368 (2019) 550–559. doi:https://doi.org/10.1016/j.jhazmat.2019.01.078.

[12] K. Ho, H. Chun, H. C. Lee, Y. Lee, S. Lee, H. Jung, B. Han, C.-H. Lee, Design of highly efficient adsorbents for removal of gaseous methyl iodide using tertiary amine-impregnated activated carbon: Integrated experimental and first-principles approach, Chem. Eng. J. 373 (2019) 1003–1011. doi:https://doi.org/10.1016/j.cej.2019.05.115.

[13] K. Ho, D. Park, M.-K. Park, C.-H. Lee, Adsorption mechanism of methyl iodide by triethylenediamine and quinuclidine-impregnated activated carbons at extremely low pressures, Chem. Eng. J. 396 (2020) 125215. doi:https://doi.org/10.1016/j.cej.2020.125215.

[14] T. L. P. Dantas, S. M. Amorim, F. M. T. Luna, I. J. S. Jr., D. C. S. de Azevedo, A. E. Rodrigues, R. F. P. M. Moreira, Adsorption of Carbon Dioxide onto Activated Carbon and Nitrogen-Enriched Activated Carbon: Surface Changes, Equilibrium, and Modeling of Fixed-Bed Adsorption, Sep. Sci. Technol. 45 (1) (2009) 73–84. doi:https://doi.org/10.1080/01496390903401762.

[15] S. Bhuvaneshwari, V. Sivasubramanian, Equilibrium, Kinetics, and Breakthrough Studies for Adsorption of Cr(VI) on Chitosan, Chem. Eng. Commun. 201 (6) (2014) 834–854. doi:https://doi.org/10.1080/00986445.2013.793674834.

[16] K. X. Lee, J. A. Valla, Investigation of metal-exchanged mesoporous Y zeolites for the adsorptive desulfurization of liquid fuels, Appl. Catal. B-Environ. 201 (2017) 359–369. doi:https://doi.org/10.1016/j.apcatb.2016.08.018.

[17] J. C. Knox, A. D. Ebner, M. D. LeVan, R. F. Coker, J. A. Ritter, Limitations of Breakthrough Curve Analysis in Fixed-Bed Adsorption, Ind. Eng. Chem. Res. 55 (16) (2016) 4734–4748. doi:10.1021/acs.iecr.6b00516.

[18] K. H. Chu, Breakthrough curve analysis by simplistic models of fixed bed adsorption: In defense of the century-old bohart-adams model, Chem. Eng. J. 380 (2020) 122513. doi:https://doi.org/10.1016/j.cej.2019.122513.

[19] A. P. Lim, A. Z. Aris, Continuous fixed-bed column study and adsorption modeling: Removal of cadmium (ii) and lead (ii) ions in aqueous solution by dead calcareous skeletons, Biochem. Eng. J. 87 (2014) 50–61. doi:https://doi.org/10.1016/j.bej.2014.03.019.

[20] Y. K. Recepoğlu, N. Kabay, I. Y. Ipek, M. Arda, M. Yüksel, K. Yoshizuka, S. Nishihama, Packed bed column dynamic study for boron removal from geothermal brine by a chelating fiber and breakthrough curve analysis by using mathematical models, Desalination 437 (2018) 1–6. doi:https://doi.org/10.1016/j.desal.2018.02.022.

[21] H. Wang, D. M. Wang, K. T. Chuang, A sulfur removal and disposal process through H_2S adsorption and regeneration: Breakthrough behaviour investigation, Process Saf. Environ. 89 (1) (2011) 53–60. doi:https://doi.org/10.1016/j.psep.2010.08.001.

[22] P. Aguilera, F. Gutiérrez Ortiz, Prediction of fixed-bed breakthrough curves for H_2S adsorption from biogas: Importance of axial dispersion for design, Chem. Eng. J. 289 (2016) 93–98. doi:https://doi.org/10.1016/j.cej.2015.12.075.

[23] T. Yamamoto, M. Tayakout-Fayolle, C. Geantet, Gas-phase removal of hydrogen sulfide using iron oxyhydroxide at low temperature: Measurement of breakthrough curve and modeling of sulfidation mechanism, Chem. Eng. J. 262 (2015) 702–709. doi:https://doi.org/10.1016/j.cej.2014.09.093.

[24] K.-J. Ko, H. Kim, Y.-H. Cho, K.-M. Kim, C.-H. Lee, Desulfurization of ultra-low-concentration H_2S in natural gas on Cu-impregnated activated carbon: Characteristics and mechanisms, Separation and Purification Technology 305 (2023) 122539. doi:https://doi.org/10.1016/j.seppur.2022.122539.

[25] CARBON, ACTIVATED, IMPREGNATED, COPPER-SILVER-ZINC- MOLYBDENUM-TRIETHYLENEDIAMINE (ASZM-TEDA), MIL-DTL-32101, U.S. ARMY EDGEWOOD CHEMICAL BIOLOGICAL CENTER (2002).

[26] M. J. Frisch, G. W. Trucks, H. B. Schlegel, G. E. Scuseria, M. A. Robb, J. R. Cheeseman, G. Scalmani, V. Barone, G. A. Petersson, H. Nakatsuji, X. Li, M. Caricato, A. V. Marenich, J. Bloino, B. G. Janesko, R. Gomperts, B. Mennucci, H. P. Hratchian, J. V. Ortiz, A. F. Izmaylov, J. L. Sonnenberg, D. Williams-Young, F. Ding, F. Lipparini, F. Egidi, J. Goings, B. Peng, A. Petrone, T. Henderson, D. Ranasinghe, V. G. Zakrzewski, J. Gao, N. Rega, G. Zheng, W. Liang, M. Hada, M. Ehara, K. Toyota, R. Fukuda, J. Hasegawa, M. Ishida, T. Nakajima, Y. Honda, O. Kitao, H. Nakai, T. Vreven, K. Throssell, J. A. Montgomery, Jr., J. E. Peralta, F. Ogliaro, M. J. Bearpark, J. J. Heyd, E. N. Brothers, K. N. Kudin, V. N. Staroverov, T. A. Keith, R. Kobayashi, J. Normand, K. Raghavachari, A. P. Rendell, J. C. Burant, S. S. Iyengar, J. Tomasi, M. Cossi, J. M. Millam, M. Klene, C. Adamo, R. Cammi, J. W. Ochterski, R. L. Martin, K. Morokuma, O. Farkas, J. B. Foresman, D. J. Fox, Gaussian˜16 Revision C.01, gaussian Inc. Wallingford CT (2016).

[27] X. Zhou, X. Li, The influence of water molecules on the stability of mineral green pigments in Chinese ancient painting, Chem. Phys. Lett. 731 (2019) 136592. doi:https://doi.org/10.1016/j.cplett.2019.136592.

[28] S. Sircar, J. Hufton, Why does the linear driving force model for adsorption kinetics work?, Adsorption 6 (2) (2000) 137–147. doi:https://doi.org/10.1023/A:1008965317983.

[29] A. Poursaeidesfahani, E. Andres-Garcia, M. de Lange, A. Torres-Knoop, M. Rigutto, N. Nair, F. Kapteijn, J. Gascon, D. Dubbeldam, T. J. Vlugt, Prediction of adsorption isotherms from breakthrough curves, Micropor. Mesopor. Mat. 277 (2019) 237–244. doi:https://doi.org/10.1016/j.micromeso.2018.10.037.

[30] T. Myers, F. Font, Mass transfer from a fluid flowing through a porous media, Int. J. Heat Mass Transf. 163 (2020) 120374. doi:https://doi.org/10.1016/j.ijheatmasstransfer.2020.120374.

[31] Z. Michalewicz, M. Schoenauer, Evolutionary Algorithms for Constrained Parameter Optimization Problems, Evol. Comput. 4 (1) (1996) 1–32. doi:https://doi.org/10.1162/evco.1996.4.1.1.

[32] L. Elliott, D. Ingham, A. Kyne, N. Mera, M. Pourkashanian, C. Wilson, Genetic algorithms for optimisation of chemical kinetics reaction mechanisms, Prog. Energ. Combust. 30 (3) (2004) 297–328. doi:https://doi.org/10.1016/j.pecs.2004.02.002.

[33] S. Katoch, S. S. Chauhan, V. Kumar, A review on genetic algorithm: past, present, and future, Multimed. Tools Appl. 80 (2021) 8091–8126. doi:https://doi.org/10.1007/s11042-020-10139-6.

[34] B. Saha, P. Chowdhury, A. Ghoshal, Al-MCM-41 catalyzed decomposition of polypropylene and hybrid genetic algorithm for kinetics analysis, Appl. Catal. B-Environ. 83 (3-4) (2008) 265–276. doi:https://doi.org/10.1016/j.apcatb.2008.02.021.

[35] G. Van Rossum, F. L. Drake, Python 3 Reference Manual, CreateSpace, Scotts Valley, CA, 2009.

[36] A. F. Gad, PyGAD: An Intuitive Genetic Algorithm Python Library (2021). arXiv:2106.06158.

[37] IBM Corp., IBM SPSS Statistics for Windows.

[38] D. A. Guzonas, D. E. Irish, A Raman and infrared spectroscopic study of triethylenediamine (DABCO) and its protonated forms, Can. J. Chem. 66 (5) (1988) 1249–1257. doi:10.1139/v88-203.

[39] T. Akutagawa, S. Takeda, T. Hasegawa, T. Nakamura, Proton Transfer and a Dielectric Phase Transition in the Molecular Conductor $(HDABCO^+)_2(TCNQ)_3$, J. Am. Chem. Soc. 126 (1) (2004) 291–294. doi:10.1021/ja0377697.

[40] F. Chalyavi, O. Adeyiga, J. M. Weiner, J. N. Monzy, A. J. Schmitz, J. K. Nguyen, E. E. Fenlon, S. H. Brewer, S. O. Odoh, M. J. Tucker, 2D-IR studies of cyanamides (NCN) as spectroscopic reporters of dynamics in biomolecules: Uncovering the origin of mysterious peaks, J. Chem. Phys. 152 (7) (02 2020). doi:10.1063/1.5138654.

[41] J. L. Pickett, M. Naderi, M. J. Chinn, D. R. Brown, The adsorption and decomposition of cyanogen chloride by modified inorganic molecular sieves, Sep. Sci. Technol. 37 (5) (2002) 1079–1093. doi:10.1081/SS-120002242.

[42] M. Naderi, J. L. Pickett, M. J. Chinn, D. R. Brown, Modified mesoporous silicates for the adsorption and decomposition of toxic gases, J. Mater. Chem. 12 (2002) 1086–1089. doi:10.1039/B110111K.

[43] D. Lin-Vien, N. B. Colthup, W. G. Fateley, J. G. Grasselli, The Handbook of Infrared and Raman Characteristic Frequencies of Organic Molecules, Academic Press, San Diego, 1991.

[44] D. Martin, Cyansäureester, I. Darstellung von Cyansäure -arylestern durch Thermolyse von Thiatriazolen, Chem. Ber. 97 (9) (1964) 2689–2694. doi:https://doi.org/10.1002/cber.19650980702.

[45] D. J. Jobe, K. C. Westaway, Fourier transform infrared spectroscopy studies of cyanide ion solutions of dimethylformamide and aqueous dimethylformamide, Can. J. Chem. 71 (9) (1993) 1353–1361. doi:https://doi.org/10.1139/v93-175.

[46] W.-J. Ong, L. K. Putri, L.-L. Tan, S.-P. Chai, S.-T. Yong, Heterostructured AgX/g-C_3N_4 (X=Cl and Br) nanocomposites via a sonication-assisted deposition-precipitation approach: Emerging role of halide ions in the synergistic photocatalytic reduction of carbon dioxide, Appl. Catal. B-Environ. 180 (2016) 530–543. doi:https://doi.org/10.1016/j.apcatb.2015.06.053.

[47] J. Nakamura, I. Nakamura, T. Uchijima, Y. Kanai, T. Watanabe, M. Saito, T. Fujitani, A Surface Science Investigation of Methanol Synthesis over a Zn-Deposited Polycrystalline Cu Surface, J. Catal. 160 (1) (1996) 65–75. doi:https://doi.org/10.1006/jcat.1996.0124.

[48] N. S. McIntyre, M. G. Cook, X-ray photoelectron studies on some oxides and hydroxides of cobalt, nickel, and copper, Anal. Chem. 47 (13) (1975) 2208–2213. doi:10.1021/ac60363a034.

[49] J. F. Moulder, W. F. Stickle, P. E. Sobol, K. D. Bomden, Handbook of X-ray Photoelectron Spectroscopy, Perkin-Elmer Corporation Physical Electronics Division, 1992.

[50] Y.-Y. Chen, Y. Zhang, W.-J. Jiang, X. Zhang, Z. Dai, L.-J. Wan, J.-S. Hu, Pomegranate-like N,P-Doped Mo_2C@C Nanospheres as Highly Active Electrocatalysts for Alkaline Hydrogen Evolution, ACS Nano 10 (9) (2016) 8851–8860. doi:10.1021/acsnano.6b04725.

[51] L. Ji, J. Wang, X. Teng, H. Dong, X. He, Z. Chen, N,p-doped molybdenum carbide nanofibers for efficient hydrogen production, ACS App. Mater. Inter. 10 (17) (2018) 14632–14640. doi:10.1021/acsami.8b00363.

[52] F. Liu, L. Csetenyi, G. M. Gadd, Amino acid secretion influences the size and composition of copper carbonate nanoparticles synthesized by ureolytic fungi, Appl. Microbiol. Biotechnol. 103 (2019) 7217–7230. doi:https://doi.org/10.1007/s00253-019-09961-2.
[53] Y. Yamada, H. Tanaka, S. Kubo, S. Sato, Unveiling bonding states and roles of edges in nitrogen-doped graphene nanoribbon by X-ray photoelectron spectroscopy, Carbon 185 (2021) 342–367. doi:https://doi.org/10.1016/j.carbon.2021.08.085.
[54] A. Majumdar, S. C. Das, T. Shripathi, R. Hippler, Chemical synthesis and surface morphology of amorphous hydrogenated carbon nitride film deposited by N_2/CH_4 dielectric barrier discharge plasma, Compos. Interface. 19 (3-4) (2012) 161–170. doi:10.1080/15685543.2012.699751.
[55] E. Bojestig, Y. Cao, L. Nyborg, Surface chemical analysis of copper powder used in additive manufacturing, Surf. Interface Anal. 52 (12) (2020) 1104–1110. doi:https://doi.org/10.1002/sia.6833.
[56] Y. Wu, X. Song, J. Zhang, S. Xu, N. Xu, H. Yang, Y. Miao, L. Gao, J. Zhang, G. Xiao, $Zn_2(C_9H_3O_6)(C_4H_5N_2)(C_4H_6N_2)_3$ MOF as a highly efficient catalyst for chemical fixation of CO_2 into cyclic carbonates and kinetic studies, Chem. Eng. Res. Des. 140 (2018) 273–282. doi:https://doi.org/10.1016/j.cherd.2018.10.034.
[57] V. R. Deitz, J. A. Rehrmann, The cumulative chemisorption of cyanogen chloride on a carbon-supported catalyst (whetlerite), Carbon 28 (2) (1990) 363–367. doi:https://doi.org/10.1016/0008-6223(90)90009-N.
[58] M. Wang, J. Zhou, S. Wu, H. Wang, W. Yang, Green synthesis of capacitive carbon derived from Platanus catkins with high energy density, J. Mater. Sci: Mater. Electron. 30 (2019) 4184–4195. doi:https://doi.org/10.1007/s10854-019-00710-9.
[59] E. Ech-chamikh, A. Essafti, Y. Ijdiyaou, M. Azizan, XPS study of amorphous carbon nitride (a-C:N) thin films deposited by reactive RF sputtering, Solar Energy Materials and Solar Cells 90 (10) (2006) 1420–1423, selected Papers from the 8th International Conference on Condensed Matter and Statistical Physics. doi:https://doi.org/10.1016/j.solmat.2005.10.007.
[60] L. Phutthatham, P. Ngernchuklin, D. Kaewpa, P. Chaiyasat, A. Chaiyasat, UV-activated coating polymer particle containing quaternary ammonium for antimicrobial fabrics, Colloid Polym. Sci. 300 (4) (2022) 351–364. doi:https://doi.org/10.1007/s00396-022-04946-6.
[61] J. Yang, Q. Yu, F.-L. Yang, K. Lu, C.-X. Yan, W. Dou, L. Yang, P.-P. Zhou, Competition and cooperativity of hydrogen-bonding and tetrel-bonding interactions involving triethylene diamine (DABCO), H_2O and CO_2 in air, New J. Chem. 44 (2020) 2328–2338. doi:https://doi.org/10.1039/C9NJ06036G.
[62] Ergun, S., Fluid Flow Through Packed Columns, Chem. Eng. Progr. 48 (2) (1952) 89–94.
URL `https://cir.nii.ac.jp/crid/1572261550410403712`
[63] M. Li, Dynamics of CO_2 adsorption on sodium oxide promoted alumina in a packed-bed reactor, Chem. Eng. Sci. 66 (23) (2011) 5938–5944. doi:https://doi.org/10.1016/j.ces.2011.08.013.
[64] G. Oh, Y. Hyun, J.-I. Choi, J. Lee, M.-K. Kim, H. Jung, Computational fluid dynamics modeling of contaminant transport with adsorption filtration inside planar-shaped air-purifying respirator canister, Chem. Eng. Res. Des. 196 (2023) 171–183. doi:https://doi.org/10.1016/j.cherd.2023.06.020.
[65] J. Thompson, Statistics for Bioinformatics: Methods for Multiple Sequence Alignment, Elsevier, 2016. doi:https://doi.org/10.1016/B978-1-78548-216-8.50011-7.
[66] H. S. Fogler, Elements of Chemical Reaction Engineering, 5th Edition, Prentice Hall, 2016.
[67] R. H. Mohammed, O. Mesalhy, M. L. Elsayed, L. C. Chow, Scaling analysis of heat and mass transfer processes in an adsorption packed bed, Int. J. Therm. Sci. 133 (2018) 82–89. doi:https://doi.org/10.1016/j.ijthermalsci.2018.07.017.

Supplemental Materials

Understanding the Catalytic Chemisorption of the Cyanogen Chloride via Breakthrough Curve and Genetic Algorithm

Jaeheon Lee[a], Jaekyung Bae[a], Junemo Koo[b], Keunhong Jeong[c], Sang Myeon Lee[a], Heesoo Jung[a], Min-Kun Kim[a,*]

[a] Chem-Bio Technology Center, Agency for Defense Development, Daejeon, 34186, Republic of Korea

[b] Department of Mechanical Engineering, Kyung Hee University, Yongin, 17104, Republic of Korea

[c] Department of Chemistry, Korea Military Academy, Seoul, 01805, Republic of Korea

[*] Corresponding author. Email: mkkim@add.re.kr (M.-K. Kim)

Table S1: Composition of the Prepared Samples with respect to carbon weight

Sample	Cu (%)	Zn (%)	Mo (%)	Ag (%)	TEDA (%)
ATAB-00000	0.0	0.0	0.0	0.0	0.0
ATAB-00005	0.0	0.0	0.0	0.0	5.0
ATAB-00010	0.0	0.0	0.0	0.0	10.0
ATAB-03000	3.0	3.0	1.2	0.030	0.0
ATAB-03005	3.0	3.0	1.2	0.030	5.0
ATAB-06000	6.0	6.0	2.4	0.061	0.0
ATAB-06005	6.0	6.0	2.4	0.061	5.0
ATAB-06010	6.0	6.0	2.4	0.061	10.0
ATAB-06015	6.0	6.0	2.4	0.061	15.0
ATAB-09000	9.0	9.0	3.6	0.091	0.0
ATAB-09005	9.0	9.0	3.6	0.091	5.0

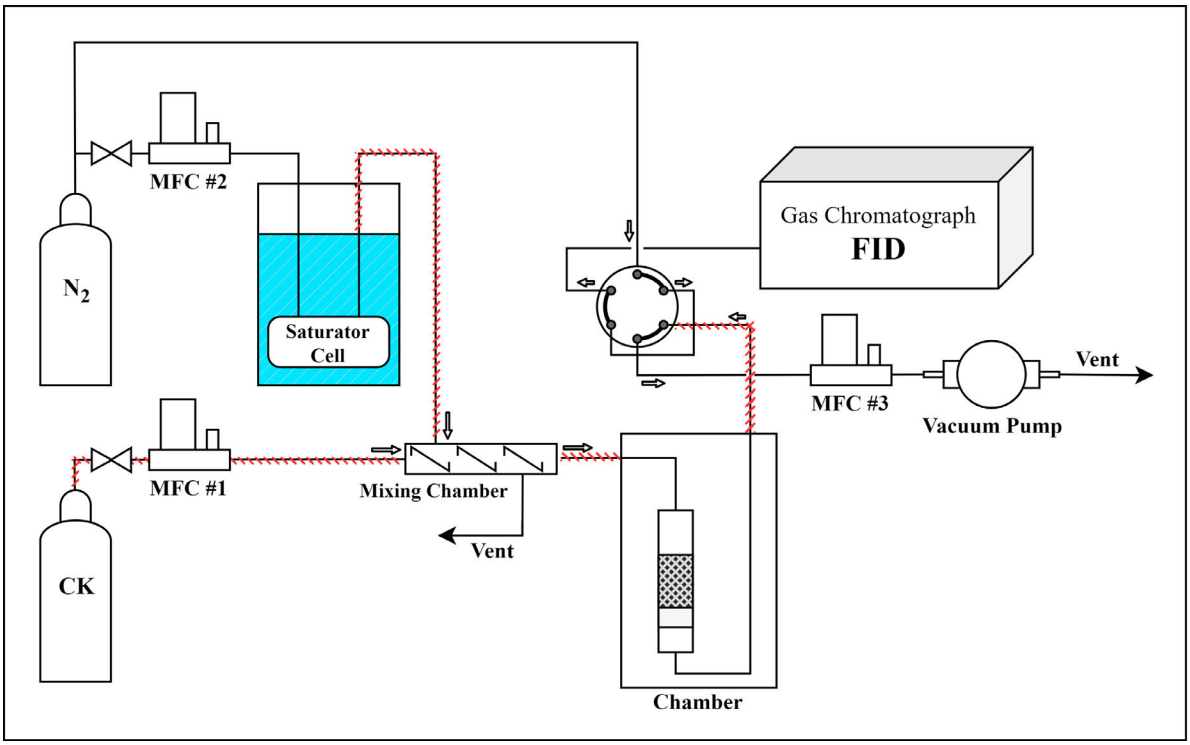

Figure S1: Schematic diagram of CK breakthrough test

Table S2: Breakthrough operating conditions.

Condition	Value
Test tube temperature	24 °C
Relative humidity	80%
Test flow rate	42.3 $mL \cdot min^{-1}$
Bed depth	2 cm
Feed Concentration	4000 $mg \cdot m^{-3}$

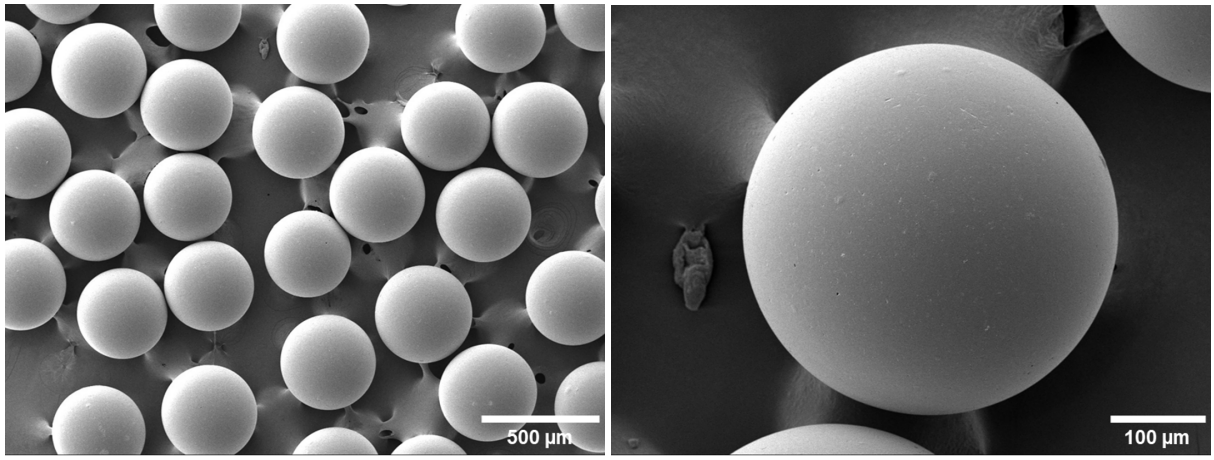

(a) **(b)**

Figure S2: SEM images of activated carbon beads at the magnitude of (a) 50 and (b) 200

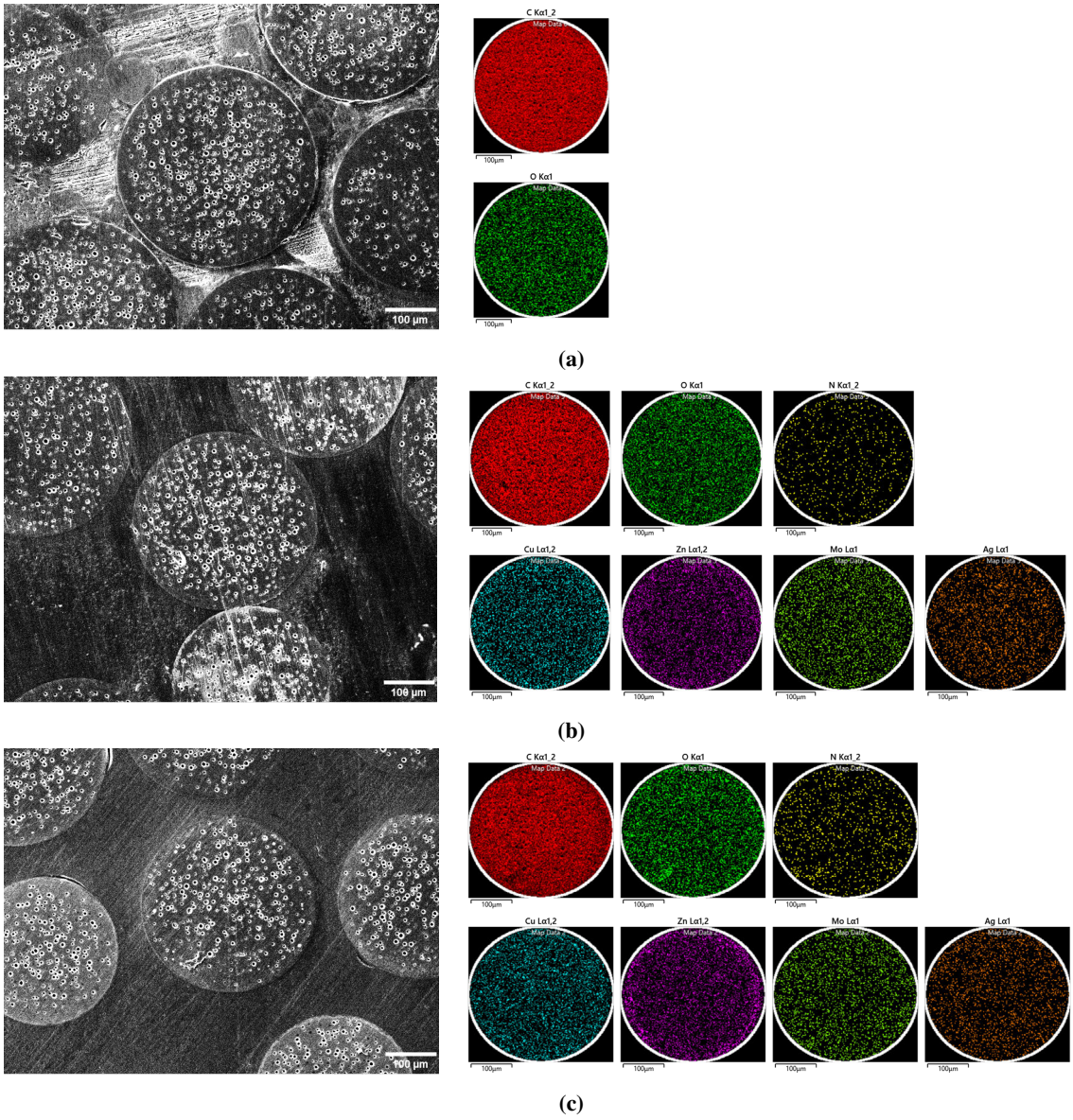

Figure S3: SEM-EDS images of polished and cold-mounted (a) activated carbon beads (b) ASZM (c) ASZM and TEDA impregnated carbon beads

Table S3: Element weight percent of each material.

Element	ATAB-00000	ATAB-06000	ATAB-06010
C	91.31 ± 0.16	78.07 ± 0.83	80.85 ± 0.87
O	8.69 ± 0.16	11.45 ± 0.27	9.81 ± 0.21
N	-	3.61 ± 1.00	4.16 ± 1.00
Cu	-	2.35 ± 0.13	2.66 ± 0.12
Zn	-	2.78 ± 0.11	2.37 ± 0.10
Mo	-	0.89 ± 0.08	0.72 ± 0.07
Ag	-	0.85 ± 0.07	0.63 ± 0.06

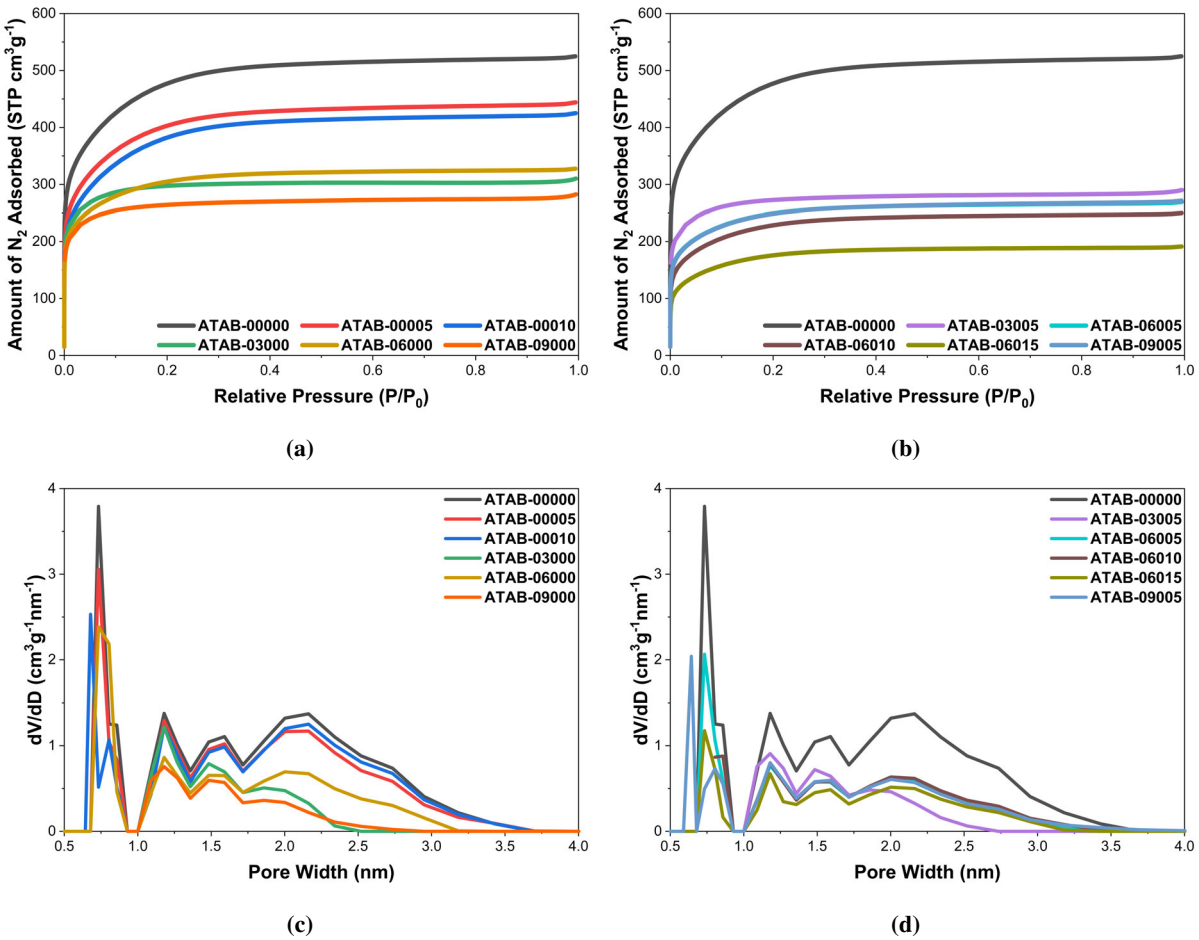

Figure S4: (a)-(b) Nitrogen adsorption isotherms at 77K and (c)-(d) pore size distributions for the materials

Table S4: Surface area and total pore volume of the samples

Sample	S_{BET} $(m^2 \cdot g^{-1})$	V_T $(cm^3 \cdot g^{-1})$
ATAB-00000	1674.45	0.81
ATAB-00005	1417.36	0.68
ATAB-00010	1327.85	0.65
ATAB-03000	1140.39	0.48
ATAB-03005	1040.16	0.45
ATAB-06000	1112.45	0.50
ATAB-06005	904.45	0.41
ATAB-06010	815.88	0.38
ATAB-06015	627.13	0.29
ATAB-09000	1011.91	0.44
ATAB-09005	903.74	0.42

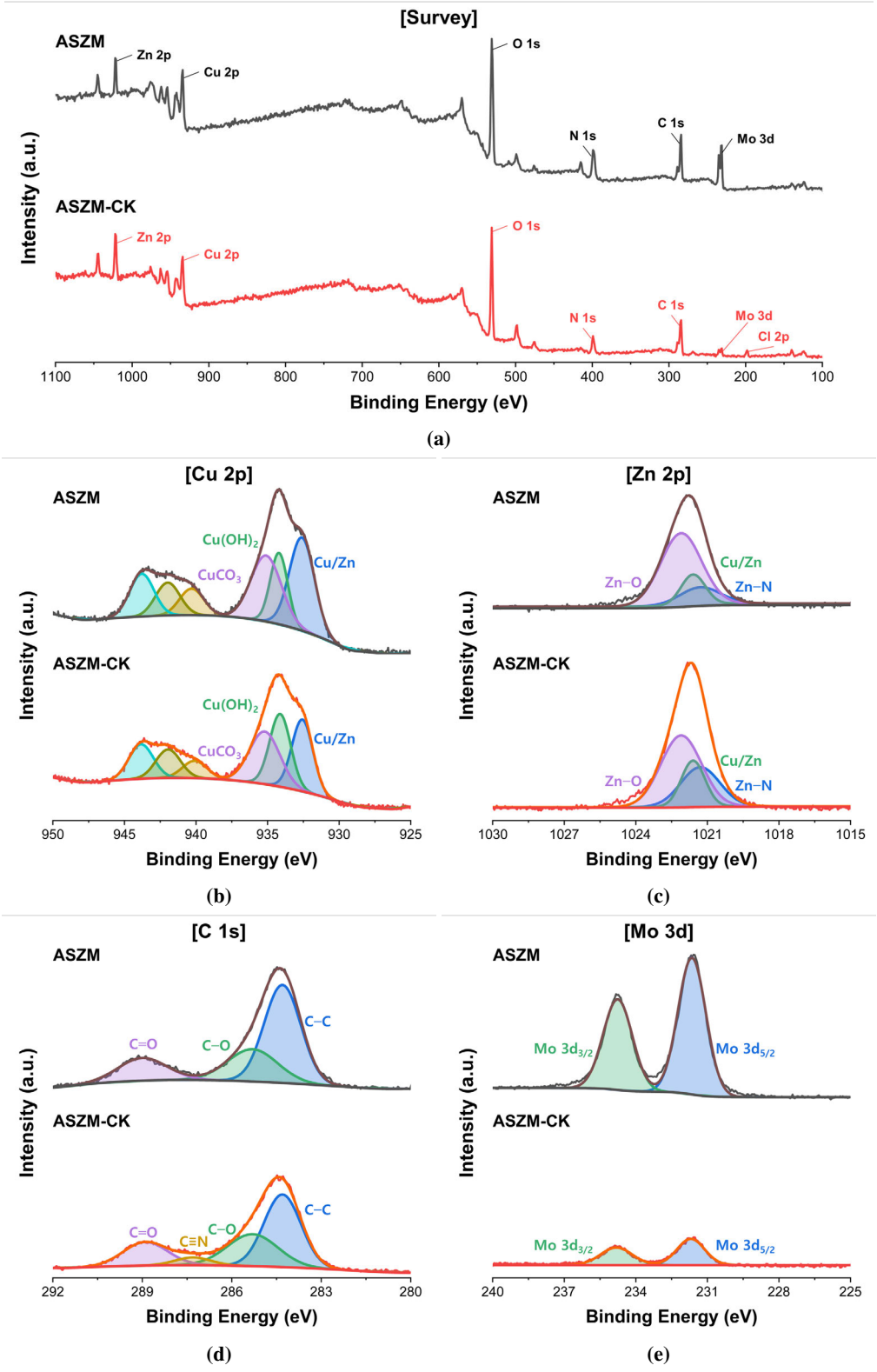

Figure S5: XPS data of dried ASZM solution powder before and after the reaction with CK

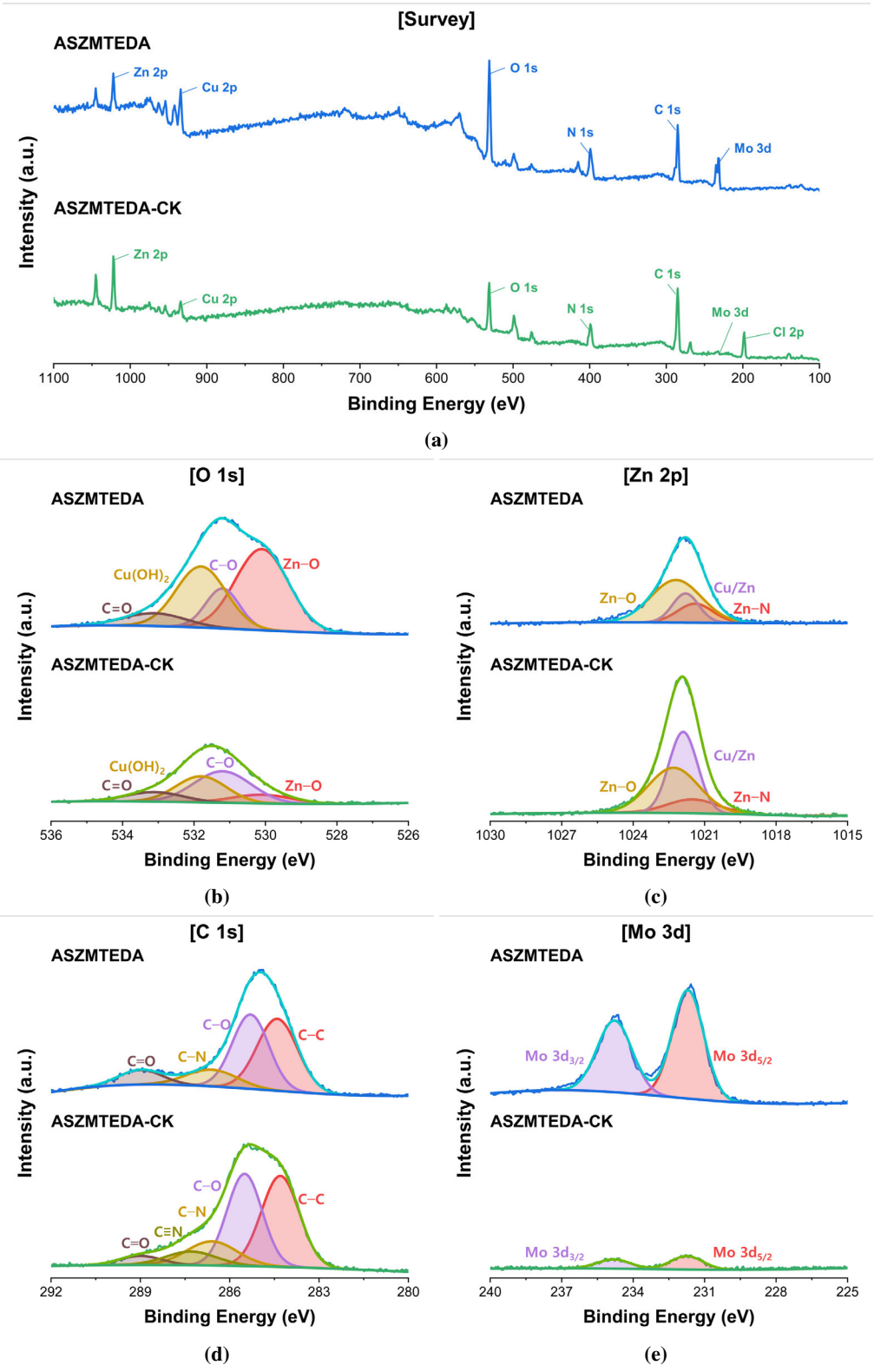

Figure S6: XPS data of TEDA-impregnated dried ASZM solution powder before and after the reaction with CK

Table S5: Pressure drop measurement result

Height (cm)	Flow ($sccm$)	Linear Velocity ($cm \cdot s^{-1}$)	Pressure Difference (Pa)
1	10	1.40	24.0
	20	2.79	35.0
	25	3.49	45.0
	30	4.19	52.0
	40	5.58	69.0
	50	6.98	83.0
2	10	1.40	46.0
	20	2.79	73.0
	25	3.49	84.0
	30	4.19	101.0
	40	5.58	129.0
3	10	1.40	78.0
	20	2.79	123.0
	25	3.49	152.0

Table S6: Mass and density of experiment samples

Sample	mass (mg)	ρ_b ($kg \cdot m^{-3}$)
ATAB-00000	131.4	550.0
ATAB-00005	155.5	650.9
ATAB-00010	154.7	647.5
ATAB-03000	157.9	660.9
ATAB-03005	176.5	738.7
ATAB-06000	167.3	700.2
ATAB-06005	190.8	798.6
ATAB-06010	198.6	831.2
ATAB-06015	218.4	914.1
ATAB-09000	162.4	679.7
ATAB-09005	201.3	842.5

Table S7: Fitted parameter based on the proposed reaction of CK with samples

Sample	D ($m^2 \cdot s^{-1}$)	k_{LDF} (s^{-1})	K_L ($m^3 \cdot kg^{-1}$)	k_{TEDA} ($m^2 \cdot g^{-1} s^{-1}$)	q^{**} ($g \cdot kg^{-1}$)	k_{metal} ($m^2 \cdot g^{-1} s^{-1}$)	k_d (s^{-1})
ATAB-00000	≈ 0	4.17×10^{-4}	2.44×10^{3}	-	-	-	-
ATAB-00005	3.89×10^{-4}	3.64×10^{-5}	4.09×10^{3}	4.46×10^{-2}	2.58×10^{1}	-	-
ATAB-00010	6.86×10^{-4}	1.58×10^{-5}	5.30×10^{3}	2.30×10^{-2}	5.08×10^{1}	-	-
ATAB-03000	≈ 0	6.63×10^{-5}	2.58×10^{3}	-	-	2.75×10^{-5}	9.65×10^{-4}
ATAB-03005	8.57×10^{-5}	8.08×10^{-6}	7.71×10^{3}	1.63×10^{-2}	1.82×10^{1}	2.23×10^{-4}	9.83×10^{-3}
ATAB-06000	≈ 0	7.63×10^{-6}	8.91×10^{3}	-	-	2.23×10^{-5}	1.37×10^{-4}
ATAB-06005	≈ 0	7.50×10^{-6}	7.29×10^{3}	7.69×10^{-3}	8.01×10^{0}	9.83×10^{-4}	8.09×10^{-3}
ATAB-06010	8.63×10^{-8}	7.20×10^{-6}	5.04×10^{3}	9.68×10^{-3}	3.52×10^{0}	6.12×10^{-4}	6.81×10^{-3}
ATAB-06015	1.29×10^{-6}	6.55×10^{-6}	2.56×10^{3}	5.18×10^{-3}	4.50×10^{0}	1.87×10^{-4}	2.11×10^{-3}
ATAB-09000	≈ 0	1.13×10^{-5}	8.85×10^{3}	-	-	1.82×10^{-5}	9.33×10^{-5}
ATAB-09005	≈ 0	7.11×10^{-6}	2.95×10^{3}	3.81×10^{-3}	8.76×10^{0}	5.01×10^{-4}	4.41×10^{-3}

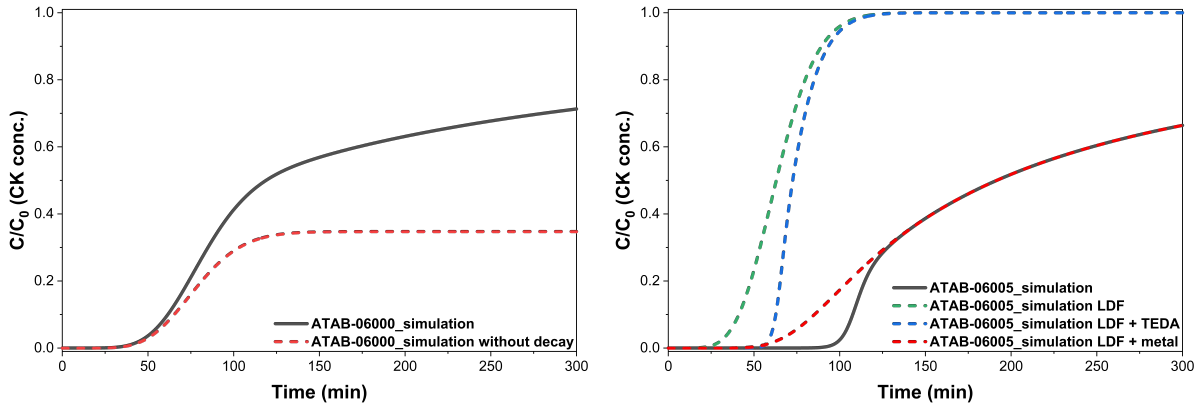

(a) **(b)**

Figure S7: (a) Catalytic deactivation effect in breakthrough curve; (b) Reaction term effect in breakthrough curve

Table S8: The Spearman's ρ correlations between fitted parameter (1-tailed)

		D	k_{LDF}	K_L	k_{TEDA}	q^{**}	k_{metal}	k_d
D	Correlation Coefficient	1	.015	-.005	**.829***	**.776****	.218	.546
	Significance Probability	-	.483	.494	**.011**	**.002**	.302	.081
k_{LDF}	Correlation Coefficient		1	-.136	**.929****	-.154	-.524	-.310
	Significance Probability		-	.345	**.001**	.326	.091	.228
K_L	Correlation Coefficient			1	.429	.042	-.310	-.167
	Significance Probability			-	.169	.451	.228	.347
k_{TEDA}	Correlation Coefficient				1	.643	.100	.800
	Significance Probability				-	.060	.436	.052
q^{**}	Correlation Coefficient					1	**.683***	**.854****
	Significance Probability					-	**.031**	**.003**
k_{metal}	Correlation Coefficient						1	**.857****
	Significance Probability						-	**.003**
k_d	Correlation Coefficient							1
	Significance Probability							-

* Correlation is significant at the 0.05 level

** Correlation is significant at the 0.01 level

Numerical analysis using Crank-Nicolson finite difference method

Nomenclature

a	: time-dependent catalytic activity
c	: gas concentration ($kg \cdot m^{-3}$)
D	: diffusivity ($m^2 \cdot s^{-1}$)
ϵ	: bed porosity
L	: bed depth (m)
k_c	: catalytic reaction rate constant ($m^3 \cdot g^{-1} s^{-1}$)
k_d	: catalyst deactivation constant (s^{-1})
k_L	: LDF model mass transfer coefficient (s^{-1})
K_L	: Linear isotherm coefficient ($m^3 \cdot kg^{-1}$)
k_T	: chemical adsorption rate constant ($kg \cdot g^{-1} s^{-1}$)
q^*	: maximum physisorbed amount on the bed per unit mass ($kg \cdot kg^{-1}$)
$\overline{q^*}$	: physisorbed amount on the bed per unit mass ($kg \cdot kg^{-1}$)
$\overline{q^{**}}$	: chemisorbed amount loading on the bed per unit mass ($g \cdot kg^{-1}$)
q_T	: maximum chemisorbed amount on the bed per unit mass ($g \cdot kg^{-1}$)
ρ_b	: bed density ($kg \cdot m^{-3}$)
u	: linear velocity ($m \cdot s^{-1}$)

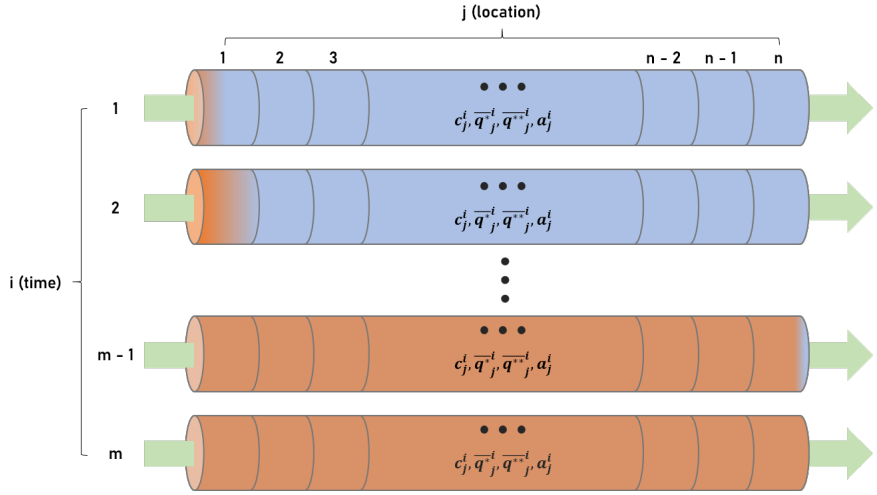

Figure S8: Basic setup for numerical analysis (Blue: unused part of the bed, Orange: used part of the bed)

The governing equation for numerical analysis is the following.

$$\frac{\partial c}{\partial t} + u\frac{\partial c}{\partial z} - D\frac{\partial^2 c}{\partial z^2} + \left(\frac{1-\epsilon}{\epsilon}\right)\rho_b \frac{\partial \overline{q^*}}{\partial t} + \rho_b \frac{\partial \overline{q^{**}}}{\partial t} + \rho_b k_c a c = 0 \tag{S1}$$

where,

$$\frac{\partial \overline{q^*}}{\partial t} = k_L(K_L c - \overline{q^*}) \tag{S2}$$

$$\frac{\partial \overline{q^{**}}}{\partial t} = k_T c(q_T - \overline{q^{**}}) \tag{S3}$$

$$\frac{da}{dt} = -k_d a^2 \tag{S4}$$

Define Crank-Nicolson parameters as follows.

$$\begin{aligned}
\frac{\partial c}{\partial t}_{(i,j)} &= \frac{c_j^{i+1} - c_j^i}{\Delta t} \\
\frac{\partial c}{\partial z}_{(i,j)} &= \frac{c_{j+1}^i - c_{j-1}^i}{4\Delta z} + \frac{c_{j+1}^{i+1} - c_{j-1}^{i+1}}{4\Delta z} \\
\frac{\partial^2 c}{\partial z^2}_{(i,j)} &= \frac{c_{j+1}^i - 2c_j^i + c_{j-1}^i}{2\,(\Delta z)^2} + \frac{c_{j+1}^{i+1} - 2c_j^{i+1} + c_{j-1}^{i+1}}{2\,(\Delta z)^2} \\
\xi_{(i,j)} &= \frac{\xi_j^{i+1} + \xi_j^i}{2};\ (\xi = c, \overline{q^*}, \overline{q^{**}}, a)
\end{aligned} \tag{S5}$$

and define additional parameters to simplify the equations.

$$\alpha = \frac{u\Delta t}{4\Delta z};\ \beta = \frac{k_L \Delta t}{2};\ \gamma = \frac{k_d \Delta t}{4};\ \delta = \beta \frac{1-\epsilon}{\epsilon}\rho_b;\ \lambda = \frac{D\Delta t}{2(\Delta z)^2};\ \zeta = \frac{k_T \Delta t}{2}\rho_b \tag{S6}$$

Then the governing equations (S1-S4) can be rewritten as follows.

$$\begin{aligned}
&(\alpha - \lambda)c_{j+1}^{i+1} + \left[1 + 2\lambda + \frac{K_L\delta}{1+\beta} + \left(q_T - \overline{q^{**}}^i{}_j\right)\zeta + \rho_b k_c \left(\frac{-1 + \sqrt{8\gamma a_j^i + 1}}{4\gamma}\right)\right] c_j^{i+1} - (\alpha + \lambda)c_{j-1}^{i+1} \\
&= -(\alpha - \lambda)c_{j+1}^i + \left[1 - 2\lambda - \frac{K_L\delta}{1+\beta} - \left(q_T - \overline{q^{**}}^i{}_j\right)\zeta - \rho_b k_c \left(\frac{-1 + \sqrt{8\gamma a_j^i + 1}}{4\gamma}\right)\right] c_j^i - (\alpha + \lambda)c_{j-1}^i + \frac{2\delta}{1+\beta}\overline{q^*}^i{}_j
\end{aligned} \tag{S7}$$

$$\overline{q^*}^{i+1}{}_j = \frac{K_L\beta}{1+\beta}(c_j^{i+1} + c_j^i) + \frac{1-\beta}{1+\beta}\overline{q^*}^i{}_j \tag{S8}$$

$$\overline{q^{**}}^{i+1}{}_j = q_T\zeta(c_j^{i+1} + c_j^i) + \left(1 - \zeta(c_j^{i+1} + c_j^i)\right)\overline{q^{**}}^i{}_j \tag{S9}$$

$$a_j^{i+1} = -a_j^i + \frac{-1 + \sqrt{8\gamma a_j^i + 1}}{2\gamma} \tag{S10}$$

To solve the above governing equations, introduce the tridiagonal matrix algorithm (Thomas algorithm). The Thomas algorithm can be used for the following matrix.

$$\begin{bmatrix} b_1 & c_1 & & & 0 \\ a_2 & b_2 & c_2 & & \\ & a_3 & b_3 & \ddots & \\ & & \ddots & \ddots & c_{n-1} \\ 0 & & & a_n & b_n \end{bmatrix} \begin{bmatrix} x_1 \\ x_2 \\ x_3 \\ \vdots \\ x_{n-1} \\ x_n \end{bmatrix} = \begin{bmatrix} d_1 \\ d_2 \\ d_3 \\ \vdots \\ d_{n-1} \\ d_n \end{bmatrix} \tag{S11}$$

This matrix can be transformed as follows.

$$\begin{bmatrix} 1 & c_1' & & & 0 \\ & 1 & c_2' & & \\ & & 1 & \ddots & \\ & & & \ddots & c_{n-1}' \\ 0 & & & & 1 \end{bmatrix} \begin{bmatrix} x_1 \\ x_2 \\ x_3 \\ \vdots \\ x_{n-1} \\ x_n \end{bmatrix} = \begin{bmatrix} d_1' \\ d_2' \\ d_3' \\ \vdots \\ d_{n-1}' \\ d_n' \end{bmatrix} \tag{S12}$$

where,

$$c'_i = \begin{cases} c_i/b_i & i = 1 \\ c_i/(b_i - a_i c'_{i-1}) & i = 2, 3, 4, \cdots, n-1 \end{cases} \tag{S13}$$

$$d'_i = \begin{cases} d_i/b_i & i = 1 \\ (d_i - a_i d'_{i-1})/(b_i - a_i c'_{i-1}) & i = 2, 3, 4, \cdots, n-1 \end{cases} \tag{S14}$$

Then, the solution can be written as,

$$x_i = \begin{cases} d'_i & i = 1 \\ d'_i - c'_i x_{i+1} & i = 2, 3, 4, \cdots, n-1 \end{cases} \tag{S15}$$

So, to apply the Thomas algorithm, write the matrix form of the governing equation as,

$$\begin{bmatrix} 1 & & & & 0 \\ -(\alpha+\lambda) & 1+2\lambda+\frac{K_L\delta}{1+\beta}+\left(q_T-\overline{q^{**}}^i_2\right)\zeta+\rho_b k_c\left(\frac{-1+\sqrt{8\gamma a_2^i+1}}{4\gamma}\right) & \alpha-\lambda & & \\ & -(\alpha+\lambda) & 1+2\lambda+\frac{K_L\delta}{1+\beta}+\left(q_T-\overline{q^{**}}^i_3\right)\zeta+\rho_b k_c\left(\frac{-1+\sqrt{8\gamma a_3^i+1}}{4\gamma}\right) & \ddots & \\ & & \ddots & \ddots & \alpha-\lambda \\ 0 & & & -1 & 1 \end{bmatrix} \begin{bmatrix} c_0 \\ c_2^{i+1} \\ c_3^{i+1} \\ \vdots \\ c_{n-1}^{i+1} \\ c_n^{i+1} \end{bmatrix} =$$

$$\begin{bmatrix} 1 & & & & 0 \\ \alpha+\lambda & 1-2\lambda-\frac{K_L\delta}{1+\beta}-\left(q_T-\overline{q^{**}}^i_2\right)\zeta-\rho_b k_c\left(\frac{-1+\sqrt{8\gamma a_2^i+1}}{4\gamma}\right) & -(\alpha-\lambda) & & \\ & \alpha+\lambda & 1-2\lambda-\frac{K_L\delta}{1+\beta}-\left(q_T-\overline{q^{**}}^i_3\right)\zeta-\rho_b k_c\left(\frac{-1+\sqrt{8\gamma a_3^i+1}}{4\gamma}\right) & \ddots & \\ & & \ddots & \ddots & \alpha-\lambda \\ 0 & & & 1 & -1 \end{bmatrix} \begin{bmatrix} c_0 \\ c_2^i \\ c_3^i \\ \vdots \\ c_{n-1}^i \\ c_n^i \end{bmatrix} + \frac{2\delta}{1+\beta} \begin{bmatrix} 0 \\ \overline{q^*}^i_2 \\ \overline{q^*}^i_3 \\ \vdots \\ \overline{q^*}^i_{n-1} \\ 0 \end{bmatrix} \tag{S16}$$

If we want to calculate unknown values in position j in time $i+1$, starting from the initial condition of unknown values at time 0, RHS of equation S16 can be treated as d_n described in equation S11. Therefore, we can now solve the governing equation at time $i+1$.